12-2018

# Thermal Neutron Characterization and Dose Modeling of a Plutonium-239/Beryllium Alpha-Neutron Source

Adam Hunter Willey
*Clemson University*, ahwille@g.clemson.edu

# THERMAL NEUTRON CHARACTERIZATION AND DOSE MODELING OF A PLUTONIUM-239/BERYLLIUM ALPHA-NEUTRON SOURCE

---

A Thesis
Presented to
the Graduate School of
Clemson University

---

In Partial Fulfillment
of the Requirements for the Degree
Master of Science
Environmental Health Physics

---

by
Adam Hunter Willey
December 2018

---

Accepted by:
Dr. Nicole E. Martinez, Committee Chair
Dr. Timothy A. DeVol
Dr. Mark A. Blenner

# ABSTRACT

Determination of neutron dose can be challenging and requires knowledge of neutron energy and neutron flux. A plutonium-239/beryllium ($^{239}$PuBe) alpha-neutron source was used to irradiate bacterial samples to create neutron dose response. The goal of this project was to characterize the thermal neutron flux of the $^{239}$PuBe alpha-neutron source and model the neutron dose using version MCNPX of the Monte-Carlo N-Particle transport codes. The 37 GBq $^{239}$PuBe alpha-neutron source was placed in a neutron "howitzer," that is, a 2-ft diameter moderating barrel with four radial irradiation ports. Multi-foil activation was used at various distances to determine thermal neutron flux, which was then used to verify a MCNPX code representing the system. Dysprosium thermal foils were used with cadmium covers. The MCNPX code was then adapted for dosimetric modeling. That is, the F5 tally, with a dose function, was used in place of the F4 tally. The four irradiation ports were found to have average thermal neutron fluxes of 5334 ± 829, 2928 ± 451, 1289 ± 199, and 1211 ± 186 neutrons $cm^{-2}$ $s^{-1}$ at 3.58, 9.04, 12.8, and 13.7 cm from the $^{239}$PuBe alpha-neutron source, respectively. The adapted MCNPX code calculated theoretical total ambient dose equivalent rates of 1717 ± 90.2, 703 ± 37.0, 286 ± 15.0, and 174 ± 9.18 mrem $hr^{-1}$ at 4, 8, 14, and 18 cm from the $^{239}$PuBe alpha-neutron source, respectively. The theoretical direct (uncollided) ambient dose equivalent rates at the same distances were 837 ± 44.0, 272 ± 14.3, 100 ± 5.29, and 63.1 ± 3.32 mrem $hr^{-1}$, respectively. Rough estimates of the absorbed dose rates were made from the ambient dose

equivalent rates and a recommendation of 23.6 cm from the PuBe source was made to achieve an absorbed dose rate of roughly 10 mGy $d^{-1}$.

# DEDICATION

To my parents, for teaching me the lessons that aren't found in classrooms and textbooks. I could not ask for better role models in life, who have taught me to be honest, do what is right, and to always work hard. For all the love, lessons, and free meals, I love you.

To my girlfriend Olivia, who has supported and believed in me throughout this journey. Who has calmed me when I am stressed and stressed me out when I am calm, I love you.

# ACKNOWLEDGEMENTS

I would like to thank Dr. Nicole Martinez for supporting and mentoring me through my graduate program. I am thankful for her trust and the chance she provided me to participate in her research group. Her knowledge and guidance has been immensely helpful in completing this project.

I would like to think the members of Dr. Martinez's research group who have helped and provided support when needed.

I would like to acknowledge the members of my committee, Dr. Timothy DeVol and Dr. Mark Blenner for supporting my project. Dr. DeVol always made time in his very busy schedule to assist me with any questions or concerns I had.

I would like to think the many peers and friends that I have made in Clemson, both in and out of the classroom. They have ensured that when I look back on college, I will remember the fun times I had rather than the times I spent studying. Specifically, I would like to think Emily Murawski who made sure I made it through my undergraduate program at Clemson University. Her decision to stay for graduate school was a huge factor in my decision.

Lastly, I would like to thank the Defense Threat Reduction Agency for funding this research under award number: HDTRA1-17-0002, and the Savannah River Chapter of the Health Physics Society for the Roscoe Hall Memorial Scholarship.

TABLE OF CONTENTS

Page

Table of Contents (Continued) Page

Table of Contents (Continued) Page

LIST OF TABLES

Page

List of Tables (Continued) Page

LIST OF FIGURES

Page

List of Figures (Continued) Page

List of Figures (Continued) Page

# CHAPTER ONE

# INTRODUCTION

## 1.1 MOTIVATION/JUSTIFICATION

Detection, and distinction, of activities related to the nuclear fuel cycle and weapons development is critical for supporting nuclear compliance as well as ensuring adequate preparation for chemical, biological, radiological, nuclear, and explosives (CBRNE) operations. The work described herein is part of a larger effort to discern the response of environmental microorganisms to different radiation types (e.g., alpha, beta, gamma, neutron) in an effort to provide the fundamental science necessary to develop radiosensitive biosensors; bacteria found ubiquitously in the environment have the potential to make excellent sentinels of clandestine nuclear activities.

The primary goal at this stage is to assess if changes in microbial transcription can be utilized to discriminate between types of radiation to which an environmental system was exposed. Currently, we are considering a bottom-up approach by first exposing bacteria to different types of radiation and comparing the responses. Relating the response of these microorganisms to their exposure requires an accurate and credible dose-response model, which in turn necessitates reasonably accurate dose determination. This work ultimately provides a dose-response model for neutron absorbed dose rate to bacterial samples housed in a neutron howitzer.

CHAPTER TWO

BACKGROUND

## 2.1 ALPHA-NEUTRON SOURCES

There are many types of neutron sources including isotopic alpha-neutron sources, gamma-neutron sources, spontaneous fission neutron sources, fission reactors, and accelerators. Isotopic alpha-neutron (α,n) sources, such as the one used in this work, are commonly encountered in research due to their low cost and availability [1].

### *2.1.1 Theory*

An alpha-neutron source consists of an alpha emitting radionuclide and a light element target. Alpha particles produced in an alpha-neutron source interact with the light element target atoms. The nucleus of the target atom absorbs the incident alpha particle and creates an excited isotope. Depending on the energy of the incident alpha particle, the excited isotope may de-excite through the release of a neutron [2]. Using beryllium-9 ($^{9}$Be) as an example target, the reaction describing this is:

$$ {}^{4}_{2}\alpha + {}^{9}_{4}\mathrm{Be} \rightarrow {}^{13}_{6}\mathrm{C}^{*} \rightarrow {}^{12}_{6}\mathrm{C} + {}^{1}_{0}n $$

The radionuclide and target components of an alpha-neutron source are combined in a homogenous mixture as a powder and compressed into a cylindrical shape. This mixture is then encapsulated in two layers of stainless steel welded together. The steel containment of the material acts as shielding for the alpha particles, allowing only neutrons and associated gamma-rays to be emitted [3]. Figure 2.1 shows the described configuration.

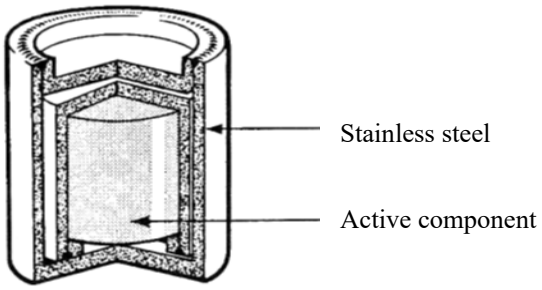


*Figure 2.1. Typical double-walled PuBe source configuration [3].*

Alpha particles produced in the source lose various amounts of energy (e.g., through self-attenuation) before interacting with the target nucleus. Neutrons emitted from compound nuclei also lose various amounts of energy through elastic collisions. Consequently, alpha-neutron sources produce neutrons with a continuous energy spectrum, as depicted below in Figure 2.2.

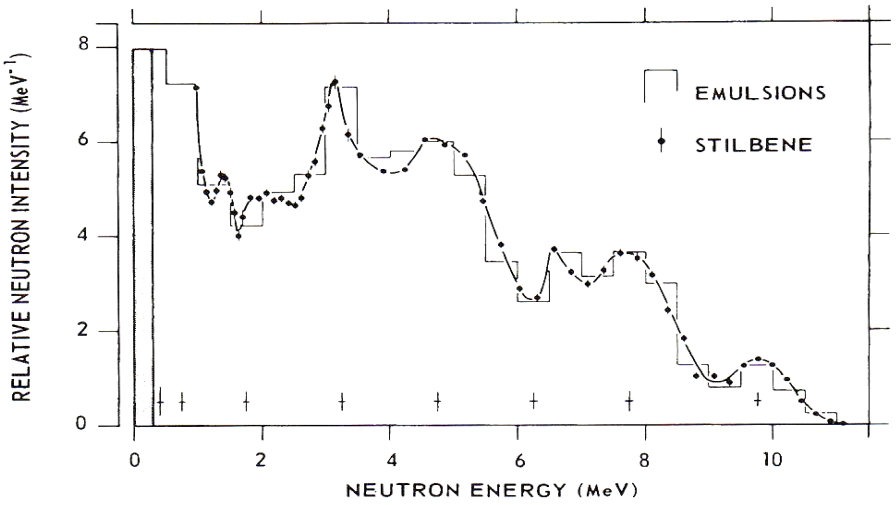


*Figure 2.2. Neutron energy spectrum of a PuBe source with 80 g of Pu [4].*

The spectrum in Figure 2.2 was produced by a plutonium/beryllium (PuBe) alpha-neutron source, but sources containing other alpha-emitting radionuclides produce similar spectra. The main source of variability in such spectra comes from the differences between primary alpha energies of the source radionuclides [4].

### *2.1.2 History*

Some of the first alpha-neutron sources used radium-226 ($^{226}$Ra), polonium-210 ($^{210}$Po), or actinium-227 ($^{227}$Ac) as the radionuclide component as all three of these isotopes are naturally occurring; $^{210}$Po and $^{226}$Ra belong to the uranium-238 decay series and $^{227}$Ac belongs to the uranium-235 decay series. However, each of these isotopes also have a drawback. For example, $^{210}$Po decays to stable lead-206 with a half-life of 138.4 days, leading to a short useful life. Additionally, although $^{226}$Ra and $^{227}$Ac have high neutron yields, their decay chains produce high intensity and high energy gamma-rays which necessitated additional shielding and safety considerations.

Nuclear research shifted focus to weapons development during the Manhattan Project and Cold War, and new radioisotopes, including plutonium-239 ($^{239}$Pu) and americium-241 ($^{241}$Am), were discovered [1]. Due to lower gamma-ray energies and longer useful lives, $^{239}$Pu and $^{241}$Am were effective alternatives to the early conventional radionuclides, particularly as large quantities of alpha-neutron sources needed to be produced to supply the growing demand.

Many light elements are suitable targets for alpha-neutron sources, including lithium (Li), boron (B), fluorine (F), and beryllium (Be). However, Be was shown to produce a significantly higher neutron yield than other light elements, so it has since been adopted as the primary target element in alpha-neutron sources [3,5]. Table 2.1 shows a comparison of the target elements when interacting with alpha particles at energies around that of $^{241}$Am (5.48 MeV) and $^{239}$Pu (5.14 MeV).

*Table 2.1. Neutron yields of common targets.*

| Elemental Target | Reaction | Alpha Energy [MeV] | Neutron Yield per $10^6$ Alpha Particles |
|---|---|---|---|
| Boron | $^{10}B(\alpha, n)$ | 5.00 | 3.552 |
| | $^{10}B(\alpha, n)$ | 5.50 | 5.674 |
| Fluorine | $^{19}F(\alpha, n)$ | 5.00 | 4.394 |
| | $^{19}F(\alpha, n)$ | 5.50 | 7.746 |
| Lithium | $^{7}Li(\alpha, n)$ | 5.00 | 0.680 |
| | $^{7}Li(\alpha, n)$ | 5.50 | 2.325 |
| Beryllium | $^{9}Be(\alpha, n)$ | 5.00 | 49.43 |
| | $^{9}Be(\alpha, n)$ | 5.50 | 71.81 |

** Data from Neutron Yields from Alpha-Particle Bombardment [5].*

As radiation source security and regulation increased, alpha-neutron sources were retired and replaced with alternatives, such as spontaneous fission neutron sources, fission reactors, and accelerators. Today, alpha-neutron sources are primarily used in research when a portable neutron source is desired [1].

## 2.2 MULTI-FOIL ACTIVATION METHOD

Knowledge of the neutron flux produced by an alpha-neutron source is important for many applications including measurement of neutron cross-sections, neutron activation analysis (NAA), dose-response analyses, as well as others. Neutrons are produced in an alpha-neutron source with energies ranging between $5\times10^{-11}$ MeV and 20 MeV in a continuous spectrum (e.g., Figure 2.2). A few different methods have been used in literature to determine neutron energy spectra of neutron sources, including the $k_0$ method, Bonner spheres, and the multi-foil activation method. The multi-foil activation method relies on indirect measurements of neutron flux through activation of foil atoms [6]. Multi-foil activation was chosen for this work (see section 4.1.4 for details of associated

calculations) due to the limited information on source composition and the geometry of the irradiation setup, which would not accommodate the Bonner spheres due to their size.

### *2.2.1 Theory*

As a neutron travels through a foil, there is a chance that it will interact with atoms within the foil. The probability of an interaction is quantified by the total neutron cross-section ($\sigma$). The traditional units of cross-section are barns (b), or $10^{-24}$ $cm^2$ [7]. The total neutron cross-section varies across neutron energies, as depicted in Figure 2.3 for indium-115 ($^{115}In$).

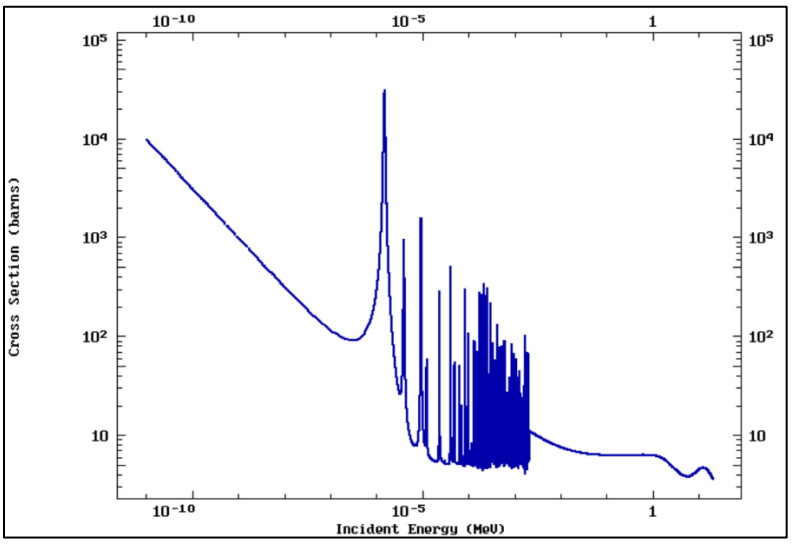


*Figure 2.3. Total neutron cross-section of $^{115}In$ plotted against neutron energy [8].*

Depending on the energy of the incident neutron, different interactions may occur including (n,γ), (n,p), (n,α), and (n,2n) reactions. This work focuses on thermal absorption which is the result of (n,γ) reactions [9].

Thermal absorption, or neutron capture, by a foil atom ( ${}^{A}_{Z}P$ ) produces a radionuclide ( ${}^{A+1}_{Z}D$ ) in the following reaction:

$$ {}^{1}_{0}n + {}^{A}_{Z}P \rightarrow {}^{A+1}_{Z}D + \gamma $$

The activity of the resulting radionuclide is determined by counting the activated foils with a beta counter or through gamma-ray spectroscopy, as radionuclides produced by neutron capture undergo beta decay with the release of associated gamma-rays. Activity is then related back to neutron flux (see Section 4.1).

### *2.2.2 Foil Materials*

There are many different materials used in foil activation. Each falls into one of three groups: thermal foils, resonance foils, and threshold foils. Thermal foils are made of specific materials that have high neutron capture cross-sections at thermal neutron energies. For this work, thermal neutrons are defined as neutrons with an energy at, or below, 0.5 eV. Resonance foils are used to measure flux in the epithermal region of neutron spectra. Epithermal neutrons have energies between 0.5 eV and 10 keV. By using multiple resonance foils, a spectrum can be created for neutron flux in the epithermal region. As shown in Figure 1.3, thermal foils also have high resonance peaks within the epithermal neutron range. These peaks also inadvertently cause activation of thermal foils, which can be corrected for by using cadmium (Cd) covers discussed in depth in the following section. Threshold foils are used to measure fast neutrons in the energy range 10 keV to 20 MeV. Use of these foils relies on a minimum energy, or threshold, to produce specific reactions. As with resonance foils, multiple threshold foils are used to produce a spectrum of neutron flux, but in the fast region [9]. Use of all three foil groups is ideal to fully characterize a

neutron source, but they are not always available and are expensive to produce. Considering availability, cost, and time, thermal neutron flux was chosen as the focus of this project.

Activation foils are typically produced in natural isotopic abundances with one isotope of interest. The isotope of interest is the one that produces a radioactive daughter after interacting with an incident neutron field and has a half-life that is long enough to allow accurate counting. Common thermal neutron foils are listed in Table 2.2 along with the target isotope (% abundance), associated neutron capture cross-section, and the radionuclide produced along with its half-life.

*Table 2.2. Commonly used thermal neutron foils and important properties.*[a]

| Foil Element | Target Isotope (% Abundance)[b] | Typical Foil Purity [%] | Neutron Capture Cross-Section ($\sigma_\gamma$) [b] | Radionuclide Daughter | Half-life (*T*) |
|---|---|---|---|---|---|
| Dysprosium (Dy) | $^{164}$Dy (28.18) | 99.9 | 920 | $^{165}$Dy | 139 min |
| Cobalt (Co) | $^{59}$Co (100) | 99.9 | 37.4 | $^{60}$Co | 5.27 yr |
| Copper (Cu) | $^{63}$Cu (69.17) | 99.99 | 4.5 | $^{64}$Cu | 12.8 hr |
| Gold (Au) | $^{197}$Au (100) | 99.95 | 100 | $^{198}$Au | 2.69 d |
| Indium (In) | $^{115}$In (95.71) | 99.99 | 170 | $^{116m}$In | 54 min |
| Lutetium (Lu) | $^{175}$Lu (97.41) | 99.7838 | 84 | $^{176m}$Lu | 3.67 hr |
| Manganese (Mn) | $^{55}$Mn (100) | 99.722 | 13.2 | $^{56}$Mn | 2.57 hr |
| Sodium (Na) | $^{23}$Na (100) | 99.99 | 0.54 | $^{24}$Na | 15.06 hr |
| Scandium (Sc) | $^{45}$Sc (100) | 99.8 | 26.5 | $^{46}$Sc | 85 d |
| Uranium-235 ($^{235}$U) | $^{235}$U (93)[c] | 99.94 | 575 | FP[d] | Varies[e] |

[a] *All foils and associated data from Reactor Experiments, Inc. Activation Foil Manual [9].*
[b] *Natural percent abundance of target isotopes from Isotopic Compositions of The Elements 1997 [10].*
[c] *Uranium-235 activation foils are enriched to approximately 93% [9].*
[d] *Uranium-235 foils undergo spontaneous fission following neutron capture and release various fission products.*
[e] *Half-lives of the various fission products varies.*

### *2.2.3 Cadmium Cut-off and Cadmium Ratio*

Cd has a neutron capture cross-section that is very high at low neutron energies but decreases rapidly as neutron energy increases. This rapid drop is known as the Cd cut-off. The exact value of the Cd cut-off varies between 0.025 eV and 0.69 eV in the literature, but for this project it was defined as 0.5 eV [9,11-13]. The neutron capture cross-sections for natural Cd and $^{115}$In are plotted against neutron energy in Figure 2.4.

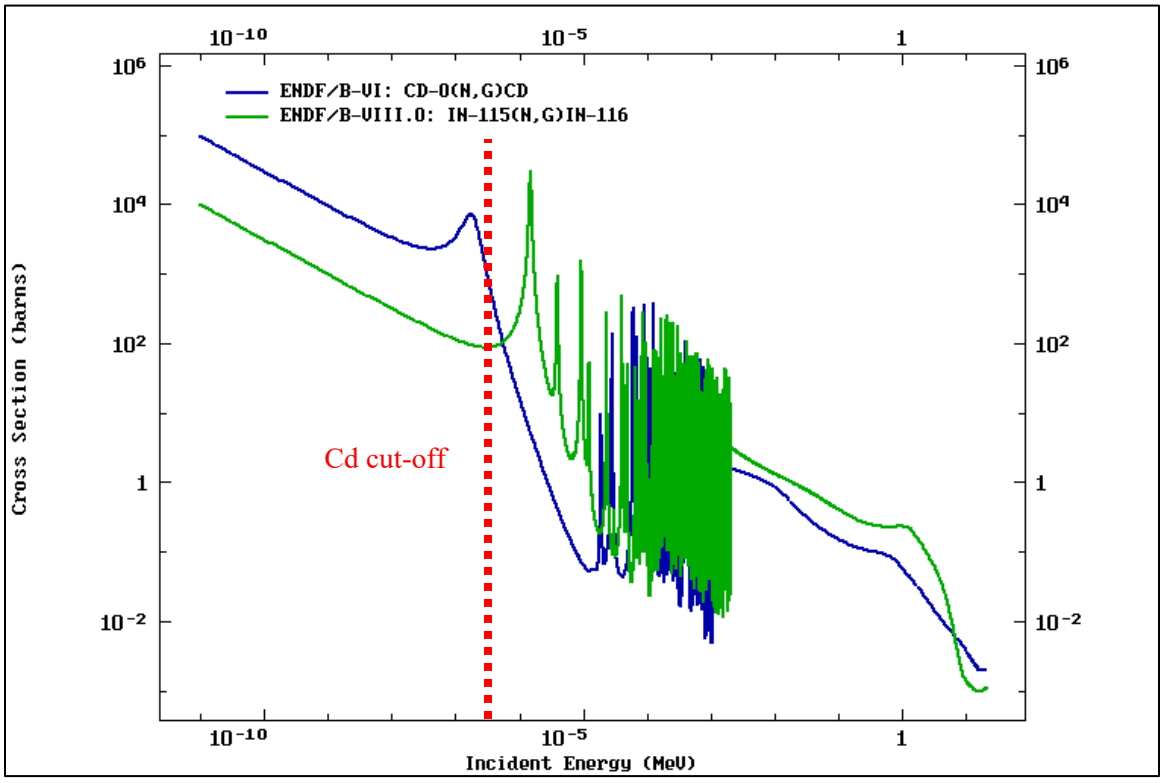


*Figure 2.4. Neutron capture cross-section vs neutron energy for Cd and $^{115}$In [8].*

Thermal foils are irradiated with and without Cd covers to calculate neutron flux below the Cd cut-off energy. Thermal foils irradiated without Cd covers are activated by thermal and epithermal neutrons to produce the bare neutron flux ($\varphi_{bare}$). Thermal foils covered by Cd are only activated by epithermal neutrons passing through the Cd cover to

produce the Cd neutron flux ($\varphi_{Cd}$) as thermal neutrons are shielded by the cover. Cd covers of a sufficient thickness stop all the neutrons with energies below the Cd cut-off, but also attenuate a portion of the epithermal neutrons that contribute to $\varphi_{Cd}$. Cadmium correction factors ($F_{Cd}$) have been determined in the literature for foils and covers of various thickness [14,15]. These $F_{Cd}$ values correct the $\varphi_{Cd}$ for the attenuated epithermal neutrons. The $F_{Cd}$ used in this work were determined based on foil characteristics and data from the literature; specific $F_{Cd}$ for the In and Dy foil configurations used herein were 1.296 and 2.331, respectively (see additional details in Section 4.1.1) [15]. With this correction factor, subtracting $\varphi_{Cd}$ from $\varphi_{bare}$ leaves the flux due only to thermal neutrons ($\varphi_{th}$), described by the Cd difference (*CD*) in Eqn. 2.1.

$$\varphi_{th} = CD = \varphi_{bare} - \varphi_{Cd} \cdot F_{Cd} \tag{2.1}$$

where, $F_{Cd}$ = correction factor for epithermal neutron attenuation

The level of thermalization that a neutron field has undergone is represented by the cadmium ratio (*CR*), calculated using Eqn. 2.2:

$$CR = \frac{\varphi_{bare}}{\varphi_{Cd} \cdot F_{Cd}} \tag{2.2}$$

The *CR* is a function of moderation, which is a function of the distance from the neutron source, and the foil type. A high *CR* indicates that the epithermal neutron field has been thermalized and that the thermal neutron field constitutes a larger portion of the total neutron field [9].

## 2.3 GAS-FLOW PROPORTIONAL COUNTER

Activated foils are typically counted using either gamma-ray spectroscopy or an alpha/beta counter. Gamma-ray spectroscopy allows discrimination between gamma-rays of specific energies and determination of the activity for a specific radionuclide [7]. For example, copper foil is composed of copper-63 ($^{63}$Cu) and copper-64 ($^{64}$Cu) which are both activated through neutron capture to radionuclides that undergo beta decay, $^{64}$Cu and copper-65 ($^{65}$Cu), respectively. Measuring the total activity of activated copper foil will result in an inaccurate calculation of thermal neutron flux due to differences between the neutron capture cross-sections and half-lives of the two copper isotopes. In this experiment, the thermal foils used did not require discrimination and were counted using a beta counter.

The counter used in this work was a gas flow proportional counter (GFPC), which are useful for counting alpha and beta activity. The detector of a GFPC contains a fill gas that continuously flows through it to remove impurities. Incident radiation that enters the detector ionizes gas molecules to produce a positive ion and a free electron, together called an ion pair. The detector has a wire running through the gas that is positively charged (anode) and the wall of the detector is connected to ground (cathode). Free electrons that are produced by incident radiation are pulled toward the anode causing secondary ion pairs along the way, called the Townsend avalanche [16]. Figure 2.5 demonstrates this reaction.

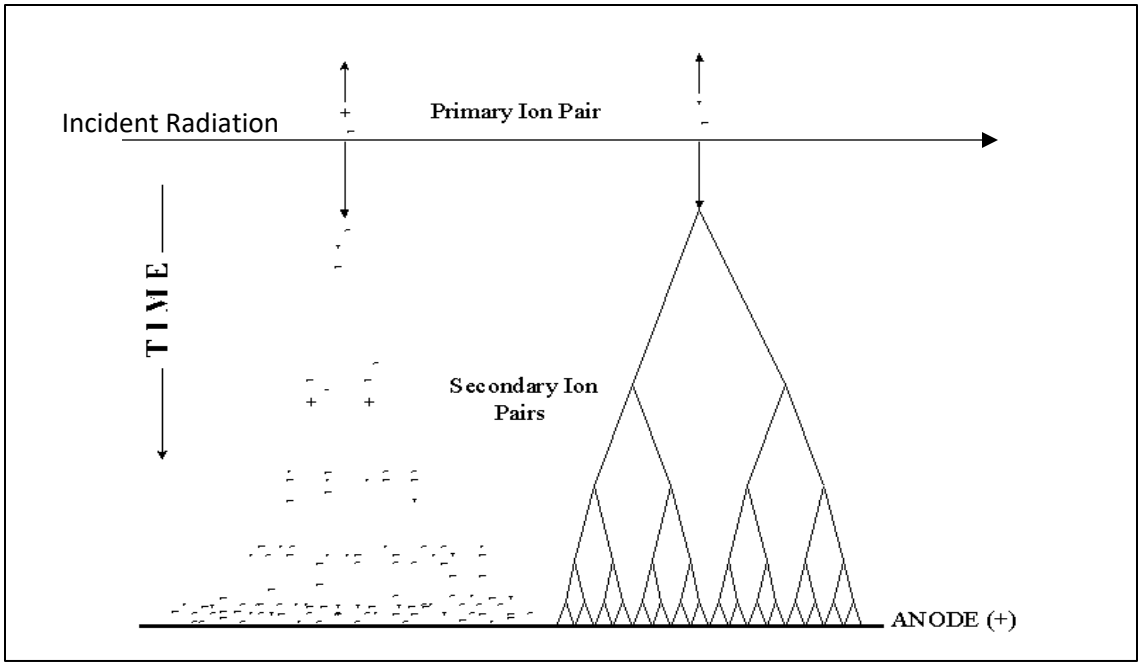


*Figure 2.5. Incident radiation interactions with GFPC fill gas [16].*

When the electrons reach the anode, a pulse is created and recorded as a count. The size of the pulse is dependent on the voltage difference that is applied to the anode and cathode and the energy deposited in the gas by incident radiation [7]. Emitted radiation that does not enter the detector, or that passes through the fill gas without ionizing the gas molecules, is not counted. The efficiency of the counter is dependent on the energy of incident radiation [17].

Incident radiation sometimes does not ionize gas molecules and instead leaves them in an excited state. These molecules then de-excite through the release of photons, which then cause their own ionizations within the fill gas. These secondary ionizations may lead to extra avalanches and pulses which leads to a loss of proportionality for the detector. Quench gases that preferentially absorb photons are added to the fill gas to solve this issue. Noble gases are commonly used in GFPC's for beta measurements, but typically require

the use of a quench gas. The most widely used gas for GFPC's is P-10, which is a mixture of 90% argon and 10% methane [16]. Methane acts as the quench gas to absorb photons produced in the detector.

## 2.4 MONTE-CARLO N-PARTICLE TRANSPORT CODE

Monte Carlo N-Particle transport code (MCNP) is the name of a set of computer codes produced by Los Alamos National Laboratory (LANL) to model physical radiation transport. User-written input files with defined geometry, materials, source information, etc. are run using MCNP to simulate radiation interactions for a defined system [18].

Different versions of MCNP have been produced at LANL since the 1940s to model gamma-ray transport (MCG), neutron transport (MCN), photon transport (MCP), as well as many other particles and interactions. Eventually the various MCNP versions were incorporated into one code, MCNP4, to simulate photon, neutron, and electron transport. In 1996, MCNP4 was adapted to include another LANL code, LAHET. This adaptation created a separate transport code, MCNPX, which can simulate all particle types at all energies. In 2002, MCNP4 was updated and rewritten in Fortran 90, resulting in MCNP5. In 2006, a merger between MCNP5 and MCNPX ultimately resulted in MCNP6 [19].

MCNP input files can be complex, often tedious, codes written by the user, and the output files contain a large amount of information to analyze. The *MCNPX User's Manual Version 2.7.0* and *An MCNP Primer* were used as the main references for learning and understanding the use of the MCNP transport code [19,20]. Appendix A contains example input files and relevant excerpts from the output files. Details of the significance of each of the cards (i.e., lines of code) can be found in the code comments.

MCNP output files provide a variety of information (both user-specified and automatic) useful for verifying the validity of the input file. This information includes the tally output (i.e., the numerical value for which the code was ultimately run) along with its associated relative error and statistical test results. Relative error ($R$) is determined internally by:

$$R = \frac{\sigma_{\bar{x}}}{\bar{x}} \tag{2.3}$$

where, $\sigma_{\bar{x}}$ = standard deviation of tally
$\bar{x}$ = mean value of the tally

Tally outputs are considered reliable if $R < 0.05$ for the F5 tally and $R < 0.1$ for all other tallies [18]. MCNP codes perform 10 statistical tests on the output data for validation and prints the test results at the end of the output file. Note that tally outputs are normalized to be per source particle and therefore represent a probability. The MCNP output must be multiplied by the number of source particles (or number of source particles per time) to convert the output to the desired units. To be considered valid, tallies must pass all 10 statistical tests and have a relative error to be considered reliable.

## 2.5 DOSE

There are many ways to describe radiation dose including absorbed dose, dose equivalent, effective dose equivalent, ambient dose equivalent, equivalent dose, and effective dose. Absorbed dose ($D$) is a physical quantity that represents the amount of energy absorbed per unit mass from incident radiation. The traditional unit of absorbed dose is rad and the modern SI unit is gray (Gy). The unit Gy is defined as 1 J $kg^{-1}$ and is equivalent to 100 rad [21].

Different radiation types (e.g. alpha, beta, gamma, neutron) cause varying amounts of biological damage. Linear energy transfer (LET) refers to the amount of energy transferred by a charged particle to the absorbing medium per unit path length traveled. LET differs between radiation types and between different energy particles of the same type. The biological damage caused by different LET radiation of the same absorbed dose is normalized using a quality factor ($Q$) to determine the dose equivalent ($H$) using Eqn. 2.4 [22].

$$H = D \cdot Q \tag{2.4}$$

The dose equivalent is a protection quantity intended to account for the relative biological effectiveness of incident radiation. Quality factors are used to normalize radiation dose to be equivalent to the biological effect of one unit of absorbed dose from low-LET radiation and are related to LET using the following relationship:

$$\begin{aligned} Q(L) &= 1 && (L < 10) \\ Q(L) &= 0.32L - 2.2 && (10 \le L \le 100) \\ Q(L) &= 300/\sqrt{L} && (L > 100) \end{aligned}$$

where $L$ is in units of keV $\mu m^{-1}$. In ICRP 60 (and updated in ICRP 103), $Q$ values were replaced with radiation weighting factors, $w_R$, which depend on radiation type and energy instead of LET [23]. The corresponding protection quantity was renamed "equivalent dose" ($H_T$) and calculated for a specific organ or tissue ($T$):

$$H_T = w_R \cdot D_{T,R} \tag{2.5}$$

Although this is the more current of these two protection quantities, it is less useful for environmental (e.g., non-human) exposures as $w_R$ are specifically for human exposure. Thus, dose equivalents are the protection quantity used in this study.

The ambient dose equivalent ($H^*(d)$) is an operational quantity that is defined as the dose equivalent that would be produced by the incident radiation field at a depth, *d*, in the International Commission on Radiation Units and Measurements (ICRU) sphere. The ICRU sphere is a phantom represented by a 30 cm diameter sphere of tissue-equivalent plastic with a density of 1 g $cm^{-3}$ that approximates the human body [24]. Operational quantities can be used to demonstrate radiation protection compliance. As defined, $w_R$ values cannot be measured, therefore $H^*(d)$ still uses the formerly recommended $Q(L)$ values [23,25]. The MCNP model used in this work produces the neutron flux through the howitzer irradiation ports. Dose conversion factors (DCF) are available in ICRP 74 to convert neutron flux to ambient dose equivalent rate at 10 mm in the ICRU sphere ($\dot{H}^*(10)$) [26].

## 2.6 LITERATURE REVIEW

Several studies in the literature have utilized alpha-neutron sources and characterization techniques similar to this work [1,6,14,27-30,47-53]. The most relevant of these are discussed below.

Bechtel (2010) proposed the use of uranium-232 ($^{232}U$) as the radionuclide component for alpha-neutron sources as an alternative to traditionally used radionuclides like $^{239}Pu$ and $^{241}Am$ [1]. Bechtel also provided a comprehensive summary of the history

and technical details of isotopic alpha-neutron sources which provided useful contextual information.

Freeman (2010) mapped the neutron flux (bare and Cd neutron flux) at 10 distances between 5 and 28 cm from the same PuBe alpha-neutron source as considered here [28]. Freeman's report provided a good foundation for this work but considered a simpler problem, therefore a more robust characterization was required for accurate dose modeling. The neutron fluxes measured by Freeman were consistent with the findings of this work.

Papastefanou (2004) measured the thermal neutron flux of a 5 Ci $^{241}$AmBe alpha-neutron source in the core of a subcritical nuclear reactor using indium thermal foils [27]. Thermal neutron flux measured by Papastefanou followed a trend similar to this work for horizontal distances from the alpha-neutron source. Due to the higher activity alpha-neutron source, findings from Papastefanou for thermal neutron flux were two orders of magnitude higher than this work.

Harvey (2010) characterized the neutron flux of a 2 Ci $^{239}$PuBe alpha-neutron source using MCNP5 and verified the simulation through neutron activation analysis in his thesis [29]. Shores (1999) calculated deep dose equivalent (DDE) rates as a function of distance for $^{238}$PuBe and $^{239}$PuBe alpha-neutron sources. DDE was defined as the dose equivalent at a tissue depth of 1 cm [30]. The DDE measured for a $^{239}$PuBe alpha-neutron source produced results similar to the findings of this report.

# CHAPTER THREE

# RESEARCH OBJECTIVES AND EXPERIMENTAL SUMMARY

The goal of this work is to determine the absorbed dose rate to bacteria at various distances from a PuBe alpha-neutron source within a neutron howitzer. The specific objectives are (1) to characterize the thermal neutron flux through four available irradiation ports within the howitzer, (2) create and verify a model of the experimental setup for neutron flux using MCNP transport code, and (3) adapt the MCNP transport code to create a dose model.

Before characterizing the thermal neutron flux, two preliminary experiments were conducted: (1) assessment of the neutron flux consistency through the four irradiation ports and (2) NAA to determine the mass of four indium (In) foils. Alpha-neutron sources are intended to be homogenous and the neutron howitzer construction was assumed to be consistent [31,32]. Therefore, it was hypothesized that neutron flux through the system was isotropic, or consistent through all four irradiation ports.

Similarly to this work, Freeman (2010) also characterized the thermal neutron flux through the irradiation ports of the howitzer using bare and Cd covered thermal foils [28]. Although the problem addressed in Freeman's report did not require a characterization as vigorous as this work, it was hypothesized that thermal neutron flux measured in this work would be similar to Freeman's findings.

MCNP transport code includes uncollided neutron flux in its output; this flux consists only of neutrons that had not undergone interactions with the howitzer media, and

therefore provides a representation of the unmoderated neutron flux produced by a neutron source. Shores (1999) used MCNP to model dose equivalent rates at various distances from an unmoderated $^{239}$PuBe alpha-neutron source and verified the model with dose measurements made by a boron trifluoride ($BF_3$) neutron detector. It was hypothesized that the $\dot{H}^*(10)$ determined from uncollided neutron flux in this work would be consistent with the results of Shores' report which are shown in Figure 3.1 [30].

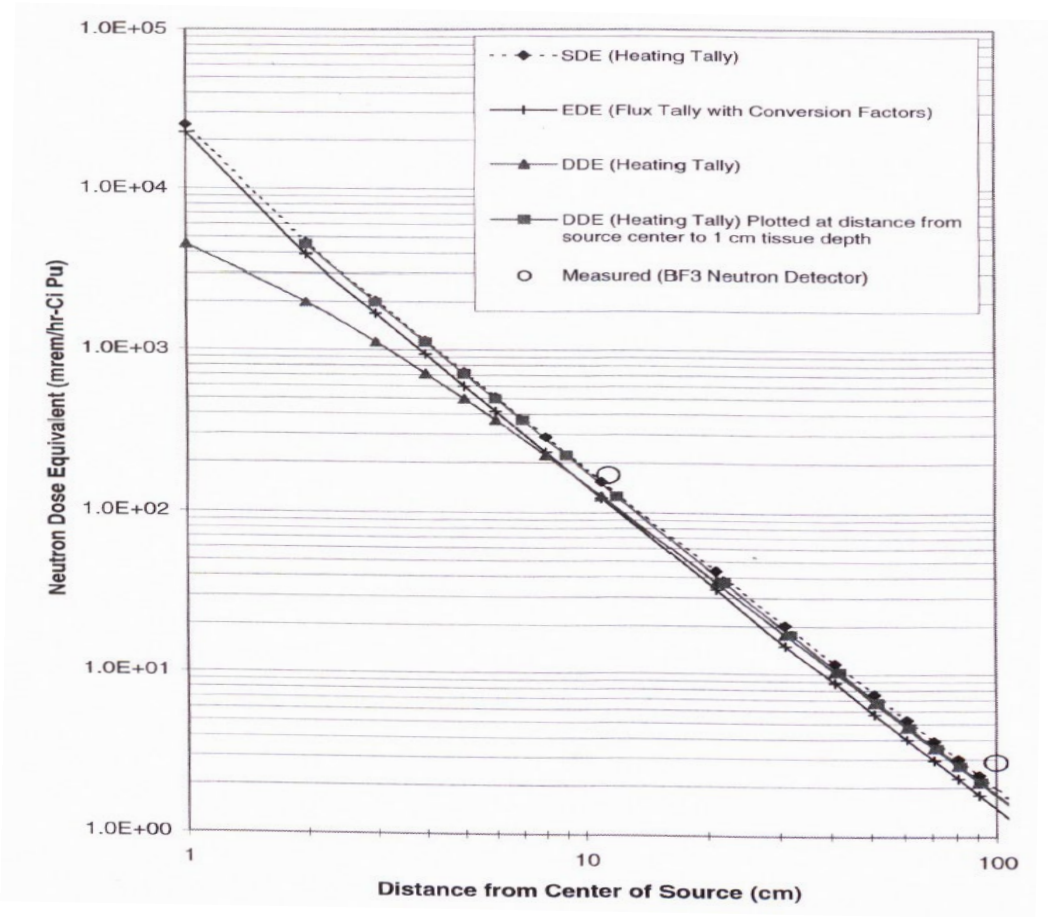


*Figure 3.1. Dose equivalent rates determined for $^{239}$PuBe sources[30].*

# CHAPTER FOUR

# MATERIALS AND METHODS

## 4.1 FLUX DETERMINATION

### *4.1.1 Experimental Set-Up*

The source of interest in this work is a 0.994 Ci $^{239}$PuBe alpha-neutron source (Serial number: MRPUBE76), hereinafter referred to as the PuBe source. The PuBe source has a double-walled configuration as described in Section 2.1.1. Although exterior capsule dimensions could be measured, the interior active material dimensions are unknown. Similar sources used by Anderson and Neff (1972) had steel thicknesses of 0.25 cm surrounding the active component [4]. Using this thickness and the exterior measurements, the dimensions of the active component were estimated and presented in Table 4.1.

*Table 4.1. PuBe source dimensions with an assumed steel thickness of 0.25 cm.*

| | Dimension [cm] | |
|---|---|---|
| | Diameter | Height |
| Exterior | 2.24 | 3.10 |
| Interior | 1.74 | 2.60 |

$^{239}$PuBe alpha-neutron sources used by other researchers have reference dates between 1957 and 1997 [33,34,35]. Based on the range of typical reference dates and the serial number, the reference date for the PuBe source was estimated to be 1976 (42 years ago).

The referenced, i.e., original, activity of the PuBe source is 0.994 Ci which is roughly 16 grams of $^{239}$Pu. The half-life of $^{239}$Pu is 24,110 years and the decay-corrected activity is 0.9928 Ci at the time of writing [36]. This determination assumes there are no

other isotopes of Pu present in the active material, but there are likely small amounts of other plutonium isotopes.

Plutonium-241 ($^{241}$Pu) undergoes beta decay and does not directly contribute to the neutron yield of a $^{239}$PuBe alpha-neutron source, but indirectly leads to an ingrowth of $^{241}$Am, which significantly increases the neutron yield. Anderson (1968) showed that a $^{241}$Pu fraction of 0.7% would result in an initial rate of increase in neutron yield of 2% per year and that the maximum increase would be roughly 33% after 69.5 years [33]. Although differences in the isotopic composition affect the neutron yield of a $^{239}$PuBe alpha-neutron source, it does not significantly impact the energy spectra produced.

Various $^{239}$PuBe alpha-neutron source compositions are discussed in the literature [33-35]. Perry and Pearson (2000) worked with a $^{239}$PuBe alpha-neutron source produced by Monsanto Chemical Company (SN: M-562) in 1959 with 94.5% $^{239}$Pu and 0.40% $^{241}$Pu by weight [34]. Nguyen (2006) determined the isotopic composition of eight $^{239}$PuBe alpha-neutron sources and found $^{239}$Pu atom percentages to be around 95% for sources produced in the late 1950s to early 1960s and around 76% for sources produced in the mid-1970s [35]. Anderson presented isotopic compositions of ten $^{239}$PuBe alpha-neutron sources produced between 1957 and 1962 with an average of 94% $^{239}$Pu and 0.48% $^{241}$Pu in weight percent [33].

No information was provided on the isotopic composition of the PuBe source used in this work, therefore the isotopic composition was assumed to be the same as sources used by Nguyen that had similar reference dates [35]. The radionuclide composition was then used to determine the Be composition in the PuBe source. Modern neutron sources

commonly have a Be to radionuclide ratio of 13:1, or $XBe_{13}$, where X is the radionuclide component [1].

The neutron yield of an alpha-neutron source is a function of the alpha activity and alpha energy. Geiger and Van der Zwan (1975) derived an empirical equation (Eqn. 4.1) that calculates a factor ($Y_\alpha$) to convert alpha-neutron source alpha activity to neutron yield. The equation is based on alpha-neutron sources with Be as the light element target.

$$Y_\alpha = 0.95 \times 0.152 E_\alpha^{3.65} \tag{4.1}$$

where, $E_\alpha$ = average alpha energy [MeV]

$Y_\alpha$ = activity to yield conversion factor [neutrons per $10^6$ alpha particles]

$^{239}$Pu has an average alpha energy of 5.14 MeV which leads to a $Y_\alpha$ of 57 neutrons per $10^6$ alpha particles. Geiger and Van der Zwan determined a $Y_\alpha$ of 57 ± 3 neutrons per $10^6$ alpha particles for $^{239}$PuBe alpha-neutron sources [37]. With $Y_\alpha$, the neutron yield ($Y$) of an alpha-neutron source can be determined using Eqn. 4.2.

$$Y = Y_a \cdot A_\alpha \cdot f \tag{4.2}$$

where, $A_\alpha$ = activity [decays per second]

$f$ = alpha emission fraction [alphas per decay]

The alpha emission fraction for $^{239}$Pu is 1.0 alpha per decay, and the corrected activity of the PuBe source was $3.673 \times 10^{10}$ Bq, or decays per second. Using the $Y_\alpha$ determined by Geiger and Van der Zwan, the calculated neutron yield of the PuBe source was $2.094 \times 10^6 \pm 1.102 \times 10^5$ neutrons per second. The calculated neutron yield assumed all alpha activity came from $^{239}$Pu, which is expected to be an underestimate of the actual neutron yield due to $^{241}$Am contributions, as well as contributions from other Pu isotopes. The neutron yield

estimated for a pure $^{239}$Pu source was used for this work initially, and later corrected with a correction factor (*CF*), described in more detail in Section 2.2.3. Note that this *CF* is specific to the work herein, intended to account for uncertainty in the source neutron yield; this is different than $F_{Cd}$ which corrects for absorption of fast or epithermal neutrons in Cd covers.

A neutron howitzer was utilized to determine neutron flux. Neutron howitzers are used to perform experiments such as neutron activation, detection, and cross-section measurements and typically consist of a cylindrical container filled with a neutron moderating material, such as water or paraffin wax, that is evenly distributed throughout [32]. Although howitzers are made in many different configurations, those used for foil activation experiments commonly consist of a source port that runs vertically from the top to the center of the container and four horizontal irradiation ports spaced 90° apart [38]. The neutron howitzer used in this work had a diameter and height of 61.0 cm, shown in Figure 4.1.

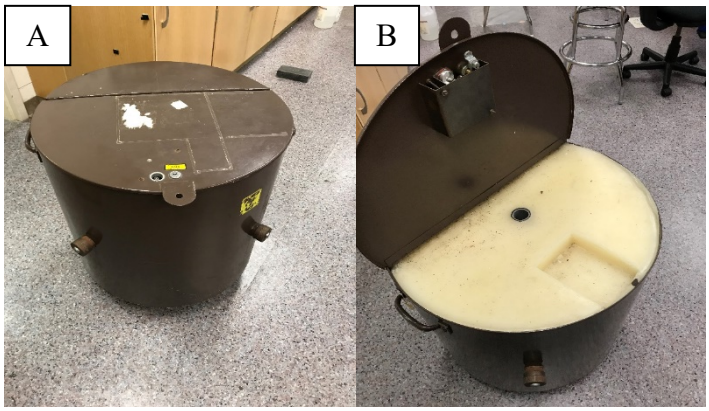


*Figure 4.1. Neutron howitzer with top closed (A) and with top opened (B).*

The container was made of 11 gauge stainless steel and filled with paraffin wax to within 0.95 cm of the top. The vertical source port (into which the PuBe source was lowered) was

made of a 31 cm long stainless steel pipe with a diameter of 4.1 cm and thickness of 0.18 cm. A PVC pipe with a 2.6 cm inside diameter and 0.34 cm thickness was cut to a length of 31 cm and placed inside the source port. The PVC pipe ensured the PuBe source was positioned in the center of the neutron howitzer. The neutron howitzer had four horizontal irradiation ports running from the bottom of the source port to the outer wall of the container. The irradiation ports were 31 cm long with a 3.8 cm diameter and 0.18 cm thickness.

Poly(methyl methacrylate) (PMMA) sleeves were used to hold activation foils for irradiation within the irradiation ports. The sleeves had an inside diameter of 3.2 cm inside of the sleeves, 3.2 cm diameter PMMA spacers were used to adjust the distance of the foils from the PuBe source. Two sized spacers were used with lengths of 2.54 cm and 3.81 cm. A set of springs and end caps were used with the sleeves to ensure activation foils remained stable and distances from the PuBe source were accurate. Figure 4.2 shows the sleeve assembly components.

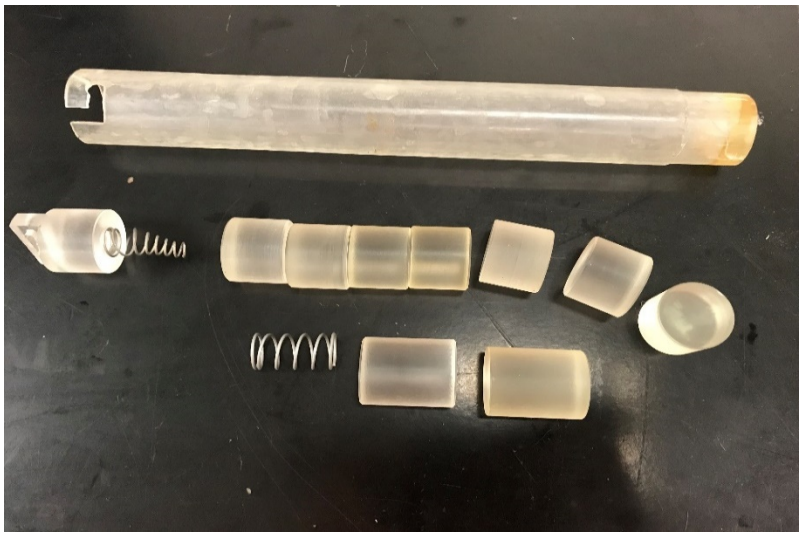

*Figure 4.2. Sleeves, spacers, springs and end caps used in the sleeve assembly.*

To confirm the material composition of the sleeves, they were tested by the Advanced Materials Lab at Clemson University using a Thermo-Nicolet Magna 550 FTIR (TNM) spectrometer equipped with a Thermo-SpectraTech Foundation Series Endurance Attenuated Total Reflection (ATR) accessory. The TNM spectrometer produced an absorbance spectrum through Fourier transform infrared spectroscopy (FTIR) that was compared to absorbance spectra in a database of organic, inorganic, and polymeric materials for identification. The material was confirmed as PMMA with the absorbance spectra in Figure 4.3.

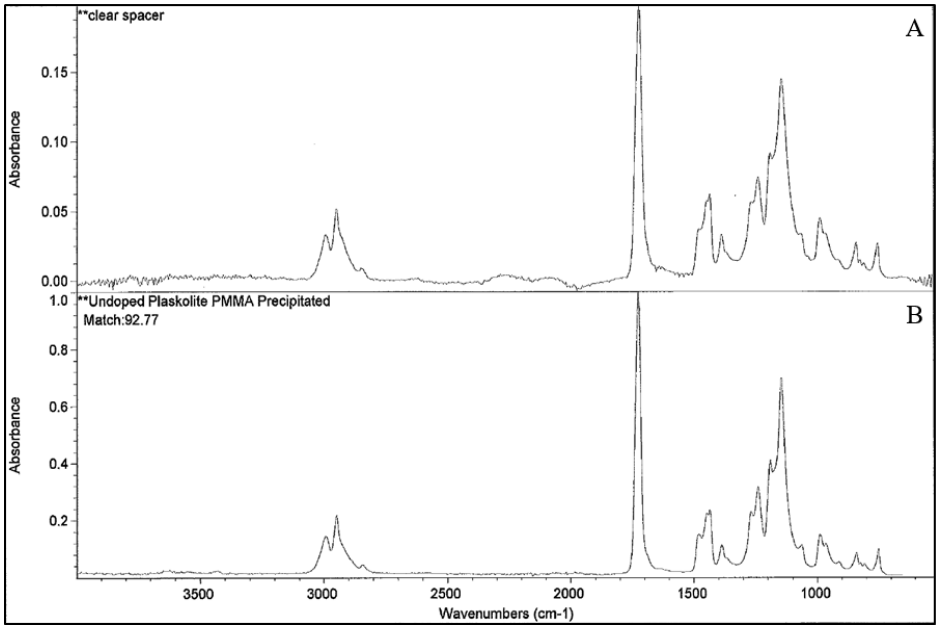


*Figure 4.3. Absorbance spectra of the sleeves (A) and of PMMA (B).*

Thermal neutron flux was characterized using four Dy foils (Shieldwerx SWX-581), and eight Cd covers (Reactor Experiments-531) (Figure 4.4). Also pictured are the In foils (Reactor Experiments-501) used for NAA.

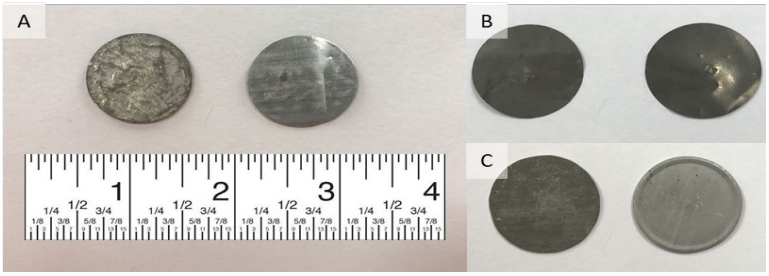


*Figure 4.4. Indium foils (A), dysprosium foils (B), and Cd covers (C).*

Table 4.2 gives the physical properties of the In and Dy foils used in this experiment [9].

*Table 4.2. Properties of indium and dysprosium foils provided by Shieldwerx, LLC [9].*

| Foil Material | Diameter [cm] | Thickness [μm] | Purity [%] |
|---|---|---|---|
| Indium (In) | 2.54 | 300[a] | 99.99 |
| Dysprosium (Dy) | 2.54 | 25.4 | 99.9 |

[a] *Total foil thickness, including indium and aluminum backing.*

The four In foils were designated as In-A, In-B, In-C, and In-D, and the four Dy foils were designated as Dy-A, Dy-B, Dy-C, and Dy-D. Indium-113 ($^{113}$In) and indium-115 ($^{115}$In) are the only two natural isotopes of In [10]. The isotope of interest is $^{115}$In due to its high thermal neutron capture cross-section and the resulting radioactive daughter from neutron capture, $^{116m1}$In. Dy has seven natural isotopes, with dysprosium-161 ($^{161}$Dy), dysprosium-162 ($^{162}$Dy), dysprosium-163 ($^{163}$Dy), and dysprosium-164 ($^{164}$Dy) having the highest abundances [10]. The target isotope in Dy foil is $^{164}$Dy, which also has a high neutron capture cross-section and a radioactive daughter, $^{165}$Dy. Eqn. 4.9 (Section 4.1.4) was used to determine the number of target atoms in the foil based on the foil mass, abundance, and atomic weight of the target isotope (Table 4.3).

*Table 4.3. Foil mass and target isotope atomic weight, abundance and number of atoms.*

| Foil | Foil Mass [mg][a] | Target Isotope | Target Abundance [atom %][b] | Atomic Weight [g mol$^{-1}$][c] | Number of Atoms [atoms] |
|---|---|---|---|---|---|
| In-A | 199.8 ± 24.4 | In-115 | 95.71 | 114.9 | $1.00\times10^{21} \pm 1.22\times10^{20}$ |
| In-B | 187.7 ± 21.5 | In-115 | 95.71 | 114.9 | $9.42\times10^{20} \pm 1.08\times10^{20}$ |
| In-C | 209.1 ± 23.1 | In-115 | 95.71 | 114.9 | $1.05\times10^{21} \pm 1.16\times10^{20}$ |
| In-D | 216.3 ± 23.3 | In-115 | 95.71 | 114.9 | $1.09\times10^{21} \pm 1.17\times10^{20}$ |
| Dy-A | 125.2 ± 0.001 | Dy-164 | 28.19 | 163.9 | $1.30\times10^{20} \pm 1.04\times10^{15}$ |
| Dy-B | 119.0 ± 0.001 | Dy-164 | 28.19 | 163.9 | $1.23\times10^{20} \pm 1.04\times10^{15}$ |
| Dy-C | 126.5 ± 0.001 | Dy-164 | 28.19 | 163.9 | $1.31\times10^{20} \pm 1.04\times10^{15}$ |
| Dy-D | 125.7 ± 0.001 | Dy-164 | 28.19 | 163.9 | $1.30\times10^{20} \pm 1.04\times10^{15}$ |

[a] *Foil masses for In were calculated using NAA; full results in Appendix B.*
[b] *Isotopic abundances taken from Isotopic Compositions of the Elements 1997 [10].*
[c] *Atomic weights taken from Atomic Weights of the Elements: Review 2000 [39].*

Dy foils did not have backing for support and masses were measured directly with a microbalance (Mettler-Toledo MX5 SN: 1125112529). In foils had an aluminum backing that provided support for the brittle material but meant the In masses had to be determined indirectly. The Dy foils were used to perform a NAA on the In foils to determine the mass of In. Appendix B contains the full results of the NAA. A mass balance was also performed using Eqn. 4.3 as a verification of the In mass in each foil.

$$m_{\mathrm{In}} = \left( \frac{\rho_{\mathrm{In}}}{\rho_{\mathrm{In}} - \rho_{\mathrm{Al}}} \right) \left( M_T - \rho_{\mathrm{Al}} r^2 \pi t \right) \tag{4.3}$$

where, $m_{\mathrm{In}}$ = mass of indium
$\rho_{\mathrm{In}}$ = density of indium = 7.31 g cm$^{-3}$ [40]
$\rho_{\mathrm{Al}}$ = density of aluminum = 2.699 g cm$^{-3}$ [40]
$M_T$ = total foil mass
$r$ = radius of foil = 1.27 cm
$t$ = total foil thickness

Masses calculated using the mass balance are reported in Appendix B. Initially, both In and Dy foils were to be used for characterization of the PuBe source thermal neutron flux.

After determining the mass of In in the foils using two methods, it was determined that the Dy foils would give more accurate results. Therefore, only Dy results were reported in this work and In results were included in Appendix C.

The total neutron capture cross-sections of $^{115}$In and $^{164}$Dy are 202 ± 2 and 2650 ± 25 barns, respectively, which include all possible neutron capture reactions; the neutron capture cross-section used in this work's various calculations (see section 4.1.4) was based on the specific activation product counted. Table 4.4 lists possible activation products of $^{115}$In and $^{164}$Dy with their associated neutron capture cross sections as well as their radiological half-lives.

*Table 4.4. $^{115}$In and $^{164}$Dy activation products with cross sections and half-lives [36,41].*

| Activation product | Capture cross section | Half-life |
|---|---|---|
| $^{116}$In | 40 ± 2 b | 14.1 s |
| $^{116m1}$In | 81 ± 8 b | 54.1 m |
| $^{116m2}$In | 81 ± 8 b | 2.16 s |
| $^{165}$Dy | 1040 ± 140 b | 2.334 h |
| $^{165m}$Dy | 1610 ± 240 b | 1.257 m |

For In foil, $^{116m1}$In is the only activation product of $^{115}$In that has a reasonable half-life. The other two activation products decayed away before they could be counted. Both activation products of $^{164}$Dy had long enough half-lives to be counted, but activated foils were counted using a beta detector which could not discriminate between the two radioisotopes. Therefore, Dy foils had to be cooled long enough to let the radioisotope with a shorter half-life decay away. The first meta-stable state of $^{116}$In ($^{116m1}$In) was the radionuclide of interest in In foil due to its longer half-life and it being a pure beta emitter. The radionuclide of interest in Dy foil was the ground state of $^{165}$Dy for the same reasons.

The eight Cd covers used in this work had a thickness of 0.50 mm and diameter of 3.17 cm. For a 0.50 mm thick Cd cover, $F_{Cd}$ for a 0.300 mm thick In foil and a 0.0254 mm thick Dy foil were 1.296 and 2.331, respectively [15].

### *4.1.2 Detection Efficiency*

An efficiency calibration was performed on the Traveler to determine the absolute detection efficiency for each relevant activation product (i.e., $^{116m1}$In and $^{165}$Dy) using promethium-147 ($^{147}$Pm), chlorine-36 ($^{36}$Cl), carbon-14 ($^{14}$C), technetium-99 ($^{99}$Tc), and strontium-90 ($^{90}$Sr)/yttrium-90 ($^{90}$Y) standards which came from Eckert & Ziegler Isotope Products (Source #: 1330-46-1 to 5; Figure 4.5).


*Figure 4.5. Eckert & Ziegler Isotope Products Beta Set calibration standards.*

Table 4.5 lists the properties of each calibration standard used, as well as the measured count rate and absolute detection efficiency ($\eta_D$) calculated using Eqn. 4.4.

$$\eta_D = \frac{\text{cpm}}{\text{dpm}} \times 100\% \tag{4.4}$$

*Table 4.5. Efficiency calibration data for the Traveler.*

| Calibration Standard | Energy [keV] | Decay Corrected Activity [Bq] | Betas per Minute [dpm] | Measured Count Rate [cpm] | Efficiency [%] |
|---|---|---|---|---|---|
| $^{147}$Pm | 224.6 | $2.92\times10^{1}$ | $1.75\times10^{3}$ | 443 ± 4.53 | 25.3 ± 0.26 |
| $^{99}$Tc | 297.5 | $3.69\times10^{2}$ | $2.22\times10^{4}$ | 9142 ± 95.8 | 41.3 ± 0.54 |
| $^{36}$Cl | 709.6 | $3.71\times10^{2}$ | $2.19\times10^{4}$ | 12347 ± 118 | 56.5 ± 0.04 |
| $^{36}$Cl* | 709.6 | $4.93\times10^{4}$ | $4.83\times10^{4}$ | 25630 ± 120 | 53.0 ± 0.43 |
| $^{14}$C | 156.5 | $3.73\times10^{3}$ | $2.24\times10^{5}$ | 33871 ± 96.7 | 15.2 ± 0.25 |
| $^{14}$C* | 156.5 | $2.89\times10^{5}$ | $2.89\times10^{5}$ | 55407 ± 166 | 19.1 ± 0.06 |
| $^{90}$Sr/Y** | 546.0/2280 | $2.92\times10^{2}$ | $1.75\times10^{4}$ | 8977 ± 19.8 | 51.2 ± 0.11 |

**Additional standards were obtained from a separate Eckert & Ziegler Isotope Product beta standard kit.*
***Data for $^{90}$Sr/Y included at the average of the two isotope's energies (i.e., 1413 keV)*

The $^{90}$Sr/Y calibration standard was assumed to be in secular equilibrium when the original activity was measured and therefore the activity of each isotope was half of the labeled activity. The original $^{90}$Sr activity was decay corrected and, again considering the $^{90}$Sr activity to be half of the total activity, used for efficiency determination. Because efficiency is dependent on energy, and $^{90}$Sr and $^{90}$Y have different energy emissions, the average of these two energies (i.e., 1413.05 keV) was used for efficiency determination of this source.

The method of least squares was used to determine a best fit equation of the form $\eta = A - \exp\left(-B \cdot E\right)$ where E is in units of keV. Specifically, Microsoft Excel Solver was used to optimize *A* and *B* such that the sum of the squares of the residuals ($SS_{res}$) was minimized. $SS_{res}$ is, in other words, the sum of the squares of the difference between the observed data and the model fit:

$$SS_{\text{res}} = \sum\left(\eta_i - \eta_{\text{fit}}\right)^2 \tag{4.5}$$

where, $\eta_i$ = observed efficiency
$n_{\text{fit}}$ = value for efficiency predicted by the model

The coefficient of determination ($R^2$) for the resultant efficiency curve was determined as

$$R = 1 - \frac{SS_{\text{res}}}{SS_{\text{tot}}} \tag{4.6}$$

where, $SS_{\text{tot}} = \sum (\eta_i - \bar{\eta})^2$ = total sum of squares

Figure 4.6 shows the observed data along with the best fit curve.

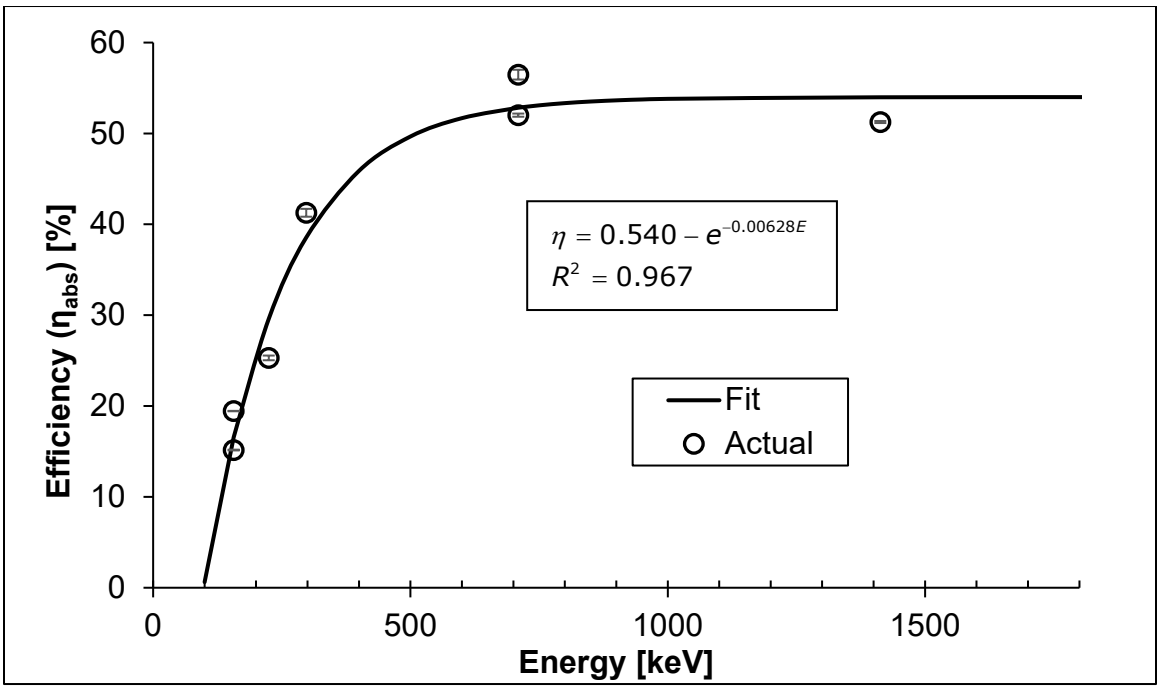


*Figure 4.6. Energy calibration curve of the Traveler.*

The calibration shows that absolute detection efficiency increases with beta energy. This agrees with expectations that as the beta energy increases, the percentage of beta particles that enter the detector volume and produce ion pairs increases. The calibration indicates that the absolute detection efficiency levels out a little above 50%, which is the theoretical maximum efficiency for the 2-pi geometry of the Traveler detector. The beta energies for $^{116m1}$In and $^{165}$Dy were 907.4 keV and 1253 keV, respectively [42]. Using the calibration curve, the absolute detection efficiency was 53.7% for $^{116m1}$In and 54.0% for

$^{165}$Dy. The efficiencies are slightly higher than 50% which may be due to elastic scattering of high energy beta particles off of the detector tray and into the detector.

### *4.1.3 Measuring Thermal Neutron Flux*

The thermal foils were placed between spacers and loaded into a sleeve in Figure 4.7.

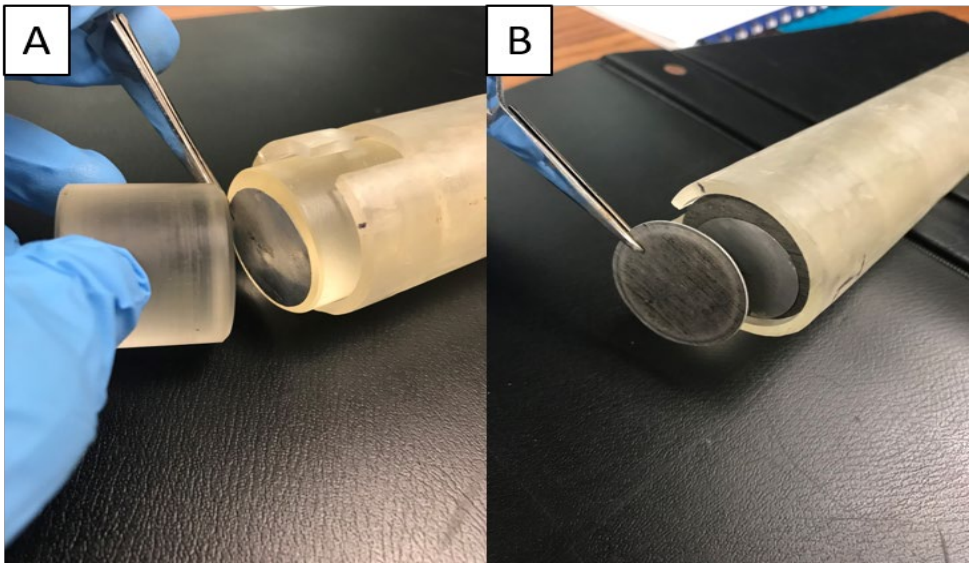


*Figure 4.7. Indium foil In-A placed between one inch spacer (A) without Cd covers and (B) with Cd covers.*

Using different combinations of spacers allowed for placement of the foils at multiple known distances. Springs were used with the sleeve caps to tightly lock spacers within sleeves and ensure a consistent distance from the PuBe source (Figure 4.8).

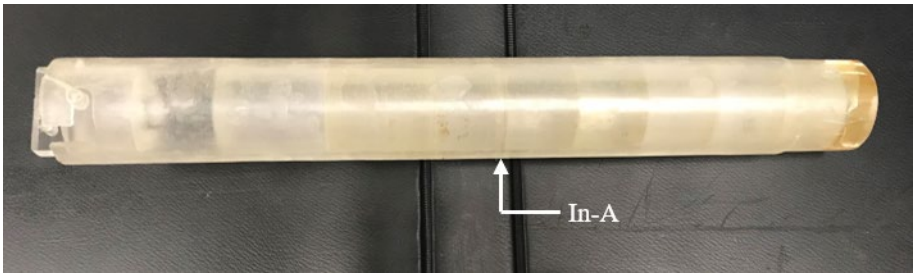


*Figure 4.8. Indium foil In-A locked in place within sleeve 1.*

Assembled sleeves were then loaded into a port and oriented the same every time by angling a mark on the sleeve downward (Figure 4.9).

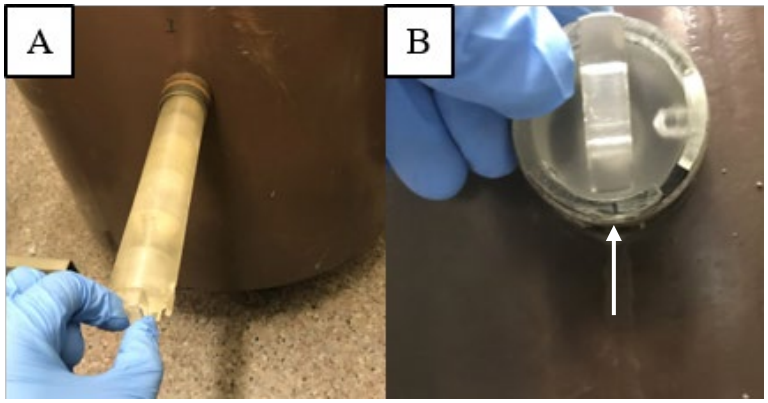


*Figure 4.9. (A) Loading sleeve 1 into port 1 and (B) checking orientation.*

Port caps were locked into place to secure sleeves in the howitzer (Figure 4.10).

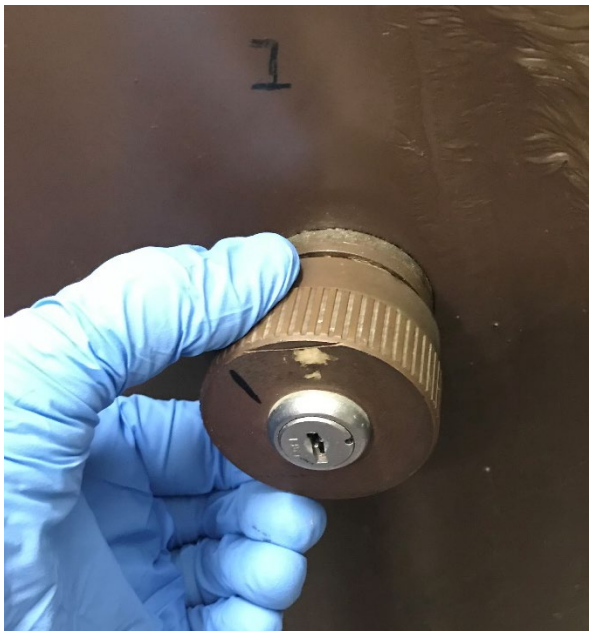


*Figure 4.10. Port cap added to port 1.*

Thermal foils were left in the irradiation ports for the desired irradiation time ($t_1$). Port caps were removed, and sleeves were unloaded at the end of $t_1$. The sleeve was disassembled,

the activated thermal foils were removed and placed in a container (Figure 4.11) for the desired cooling time ( $t_2$ ).


*Figure 4.11. Container for Dy foils.*

Activated thermal foils were counted using a GFPC, G5020 Traveler (SN: 011701), produced by Gamma Products, Inc. (Figure 4.12).


*Figure 4.12. The Traveler GFPC produced by Gamma Products, Inc.*

Activated foils were placed in the center of a detector tray, the tray was loaded into the tower, and the tower was attached to the detector (Figure 4.13).

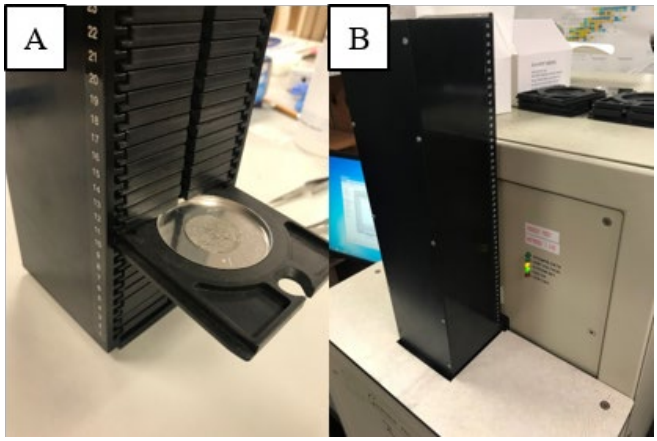


*Figure 4.13. (A) Detector tray 10 holding In-A in tower and (B) tower attached to detector.*

Detector tray 3 was always kept empty to provide a background count. Detector trays 1 and 2 held a thorium-230 and $^{99}$Tc technetium-99 source, respectively, for performing QA/QC checks. The gas tank was opened to provide gas to the detector at a flowrate between 0.15-0.20 SCFH (Figure 4.14).

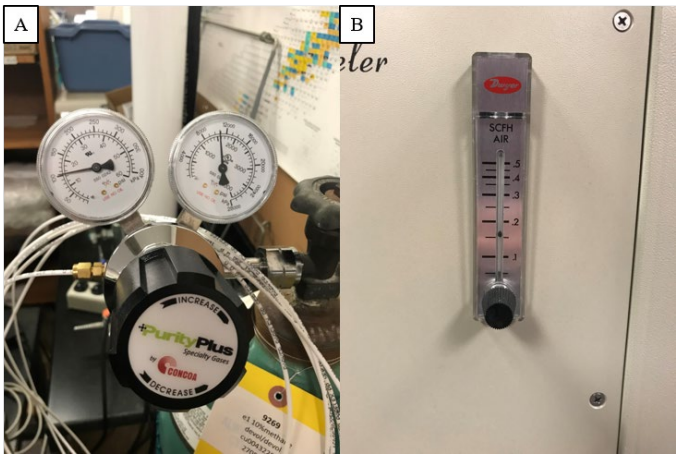


*Figure 4.14. (A) Regulator opened at the P-10 tank to (B) provide 0.16 SCFH of gas to the Traveler.*

The desired counting time ($t_3$) was set for each detector tray holding activated thermal foils, detector trays 1 and 2 were set to count for one minute each, and detector tray 3 was set to count for five minutes. The count was started at the end of $t_2$. The output from the Traveler was a beta and alpha count for each detector tray. The background count (tray 3) was divided by five minutes to get the background count rate and the count for each foil was divided by $t_3$ to get the gross count rate. The background count rate was then subtracted from the gross count rate to determine the net count rate of the activation foils. Multiplying the net count rate by $t_3$ resulted in the net count ($C_{net}$) for each thermal foil.

The Traveler was operated at an applied voltage of 1700 V and used a gas mixture of 90% argon and 10% methane, called P-10. The detector used to count samples in the Traveler is shown in Figure 4.15.

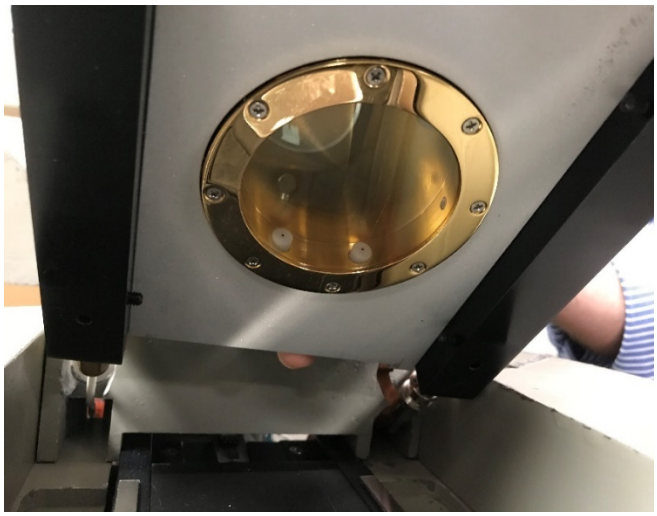

*Figure 4.15. GFPC used inside the Traveler.*

The Traveler measures energy deposition from incident alpha and beta particles as pulses. The pulses are counted to determine the activity of the sample. Alpha particles deposit large amounts of energy within the detector relative to beta particles. Therefore, a

discriminator can be set on the pulse amplitude to distinguish between alpha and beta particles. The Traveler uses a discriminator set at channel 824, where all counts between channel 1 and 824 are considered beta particles and all counts between channel 825 and 1024 are considered alpha particles. The channel number is a function of the pulse height [43].

### *4.1.4 Specific Calculations*

The activity of an activated foil sample is defined by Eqn. 4.7.

$$A_s = M \cdot \sigma \cdot \varphi \tag{4.7}$$

where, $A_s$ = saturated activity
$M$ = number of foil target atoms
$\sigma$ = neutron capture cross-section
$\varphi$ = neutron flux

Saturated activity ($A_s$) is the maximum activity that can be achieved in an activated foil sample. $A_s$ is reached with irradiation times greater than, or equal to, seven half-lives of the activation isotope. For irradiation times less than seven half-lives, the activity is corrected using Eqn. 4.8.

$$A_0 = M \cdot \sigma \cdot \varphi \cdot (1 - e^{-\lambda t_1}) \tag{4.8}$$

where, $A_0$ = activity immediately after $t_1$
$\lambda$ = decay constant of the activated foil isotope
$t_1$ = irradiation time

The number of atoms in a foil is calculated using Eqn. 4.9.

$$M = \frac{N_A \cdot m \cdot f}{W} \tag{4.9}$$

where, $N_A$ = Avogadro's number ($6.022 \cdot 10^{23}$ atoms mol$^{-1}$)
$m$ = foil mass (g)
$W$ = atomic weight of the target isotope (g mol$^{-1}$)
$f$ = mass fraction of the target isotope in the foil

The decay constant of the activated foil isotope is solved in Eqn. 4.10.

$$\lambda = \frac{\ln(2)}{T} \tag{4.10}$$

where, $T$ = half-life of the activated foil atom

In most cases, activated foils are not counted immediately following irradiation. The time between the end of irradiation and counting is commonly called the "cooling" time ($t_2$). As the foil decays, it follows the exponential decay equation (Eqn. 4.11).

$$A_1 = A_0 e^{-\lambda t_2} \tag{4.11}$$

where, $A_1$ = activity after $t_2$

Activated foils will also decay during counting. For counting times ($t_3$) that are significantly smaller than the half-life of the radioisotope, change in activity can be ignored with little error. The activity that is detected ($A'$) will not be the final or initial foil activity, but an average value over the counting time. This is found by solving the average value integral in Eqn. 4.12.

$$A' = \frac{1}{t_3}\int_0^{t_3} A_1 e^{-\lambda t} dt \tag{4.12a}$$

or,

$$A' = \frac{A_1}{t_3} \cdot \frac{1 - e^{-\lambda t_3}}{\lambda} \tag{4.12b}$$

Combining Eqn. 4.8, Eqn. 4.9, Eqn. 4.11, and Eqn. 4.12b results in the following (Eqn. 4.13):

$$A' = \frac{N_A \cdot m \cdot f \cdot \sigma \cdot \varphi \cdot (1 - e^{-\lambda t_1}) \cdot e^{-\lambda t_2} \cdot (1 - e^{-\lambda t_3})}{W \cdot t_3 \cdot \lambda} \tag{4.13}$$

The net count rate ($C_{net}$ / $t_3$) determined by a detector is related to $A'$ by Eqn. 4.14.

$$A' = \frac{C_{net}}{t_3 \cdot \eta_D} \tag{4.14}$$

where, $C_{net}$ = net counts (gross counts minus background counts for $t_3$)
$\eta_D$ = absolute detection efficiency

The neutron flux is solved for by combining and rearranging Eqn. 4.13 and Eqn. 4.14 to produce Eqn. 4.15 [27].

$$\varphi = \frac{C_{net} \cdot W \cdot \lambda}{N_A \cdot m \cdot f \cdot \eta_D \cdot \sigma \cdot (1 - e^{-\lambda t_1}) \cdot e^{-\lambda t_2} \cdot (1 - e^{-\lambda t_3})} \tag{4.15}$$

$C_{net}$, $t_1$, $t_2$, and $t_3$ were recorded for each trial and used in Eqn. 4.15 to calculate neutron flux (bare or Cd). Thermal neutron flux was calculated using Eqn. 2.1 when bare and Cd neutron flux was measured at the same distance for the same foil.

## 4.2 PRELIMINARY EXPERIMENTS

Two preliminary experiments were run including a consistency test and a NAA. Detailed results of these experiments were included in Appendix B as mentioned previously.

### *4.2.1 Initial Consistency Determination*

Flux consistency tests were run to determine if measured bare neutron flux was consistent between the four ports of the neutron howitzer. Bare neutron flux considered both epithermal and thermal neutrons and could be measured in half the time it would take to measure the thermal neutron flux. Therefore, it was considered an adequate approach to check consistency. Confirming a consistent spatial distribution would mean one dose

model could be used to describe all four ports, considerably decreasing the time needed for characterization.

Four rounds of experiments were run to assess the consistency of bare neutron flux through the irradiation ports. Measurements were made using the four In foils loaded in sleeve/spacer combinations as listed in Table 4.6. Note that each sleeve has a slightly different distance between the end and the first spacer; distances and number of spacers are reported for clarity and repeatability.

*Table 4.6. Configuration of foil loading for consistency test.*

| Foil | Sleeve | Distance between first spacer and end of sleeve [cm] | Number of spacers[a] | | Distance from source [cm] |
|---|---|---|---|---|---|
| | | | 2.54 cm | 3.81 cm | |
| In-A | 1 | 1.32 | 3 | 0 | 8.94 |
| In-B | 2 | 1.14 | 4 | 0 | 11.3 |
| In-C | 3 | 1.20 | 2 | 2 | 13.9 |
| In-D | 4 | 1.86 | 3 | 2 | 17.1 |

[a] *Number of spacers placed between foils and the PuBe source.*

The sleeves, assembled with the respective foils and spacers, were placed in the irradiation ports for each round of experiments as indicated in Table 4.7. Three trials were run in each round of experiments.

*Table 4.7. Irradiation scheme for sleeve placement in irradiation ports.*

| Sleeve | Irradiation Port | | | |
|---|---|---|---|---|
| | Round 1 | Round 2 | Round 3 | Round 4 |
| 1 | 1 | 4 | 3 | 2 |
| 2 | 2 | 1 | 4 | 3 |
| 3 | 3 | 2 | 1 | 4 |
| 4 | 4 | 3 | 2 | 1 |

The times used for each foil were kept constant for each trial (Table 4.8).

*Table 4.8. Irradiation, cooling, and counting times used for each foil.*

| | Time [min] | | |
|---|---|---|---|
| Foil | Irradiation ($t_1$) | Cooling ($t_2$) | Counting ($t_3$) |
| In-A | 60 | 78 | 15 |
| In-B | 60 | 60 | 15 |
| In-C | 60 | 42 | 15 |
| In-D | 60 | 10 | 30 |

Counting times were determined to keep error less than 1% using Eqn. 4.16.

$$\text{Error}(\%) = \frac{\sqrt{C_{net}}}{C_{net}} \times 100\% \tag{4.16}$$

A net count of 10,000 or greater is required to reach an error less than 1%. To minimize the interference of short-lived activation products, including other isotopes of In, $t_3$ was at least 10 minutes. Counting of the activated foils cannot be done simultaneously in the Traveler, which led to the different times for $t_2$. The neutron capture cross-section ($\sigma$) for activation to $^{116m1}$In was used in Eqn. 4.15 to find neutron flux.

One-way analysis of variance (ANOVA) statistical tests were conducted for each foil distance to determine the significance of the port number on neutron flux. Significance was taken as $p < 0.05$. A significant p-value indicates rejection of the null hypothesis of equal means between the four ports and indicates that there is a statistically significant difference between flux values of at least one of the ports. All statistical analyses were conducted with Minitab (Minitab18, State College, PA, U.S.).

The above procedure was repeated while a motor was mounted to rotate the PuBe source. A similar method was used by Cooper and Kabir (1972) with a decrease in uncertainty from 20% to 1% for threshold detectors [44]. The results of each set of

experiments are displayed in Appendix B. The results indicated the flux through the four irradiation ports was consistent and the use of the motor was not necessary.

### *4.2.2 Neutron Flux Spatial Distribution*

The neutron howitzer was fit with a motor to rotate the PVC insert in the source port during initial tests on the isotropy of the system, shown in Figure 4.16.

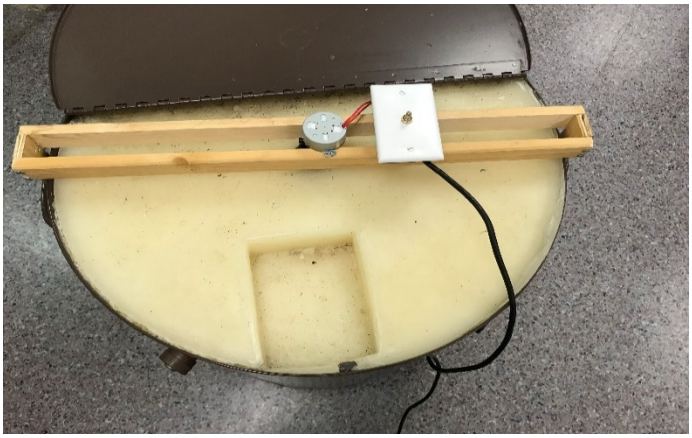

*Figure 4.16. Neutron howitzer with motor assembly attached to rotate the source port.*

A 110V AC 4W CHANCS motor (TYC-50) was used to rotate the PVC insert at 18 rpm. A rubber expansion plug was attached to the motor shaft using a coupling (Figure 4.17).

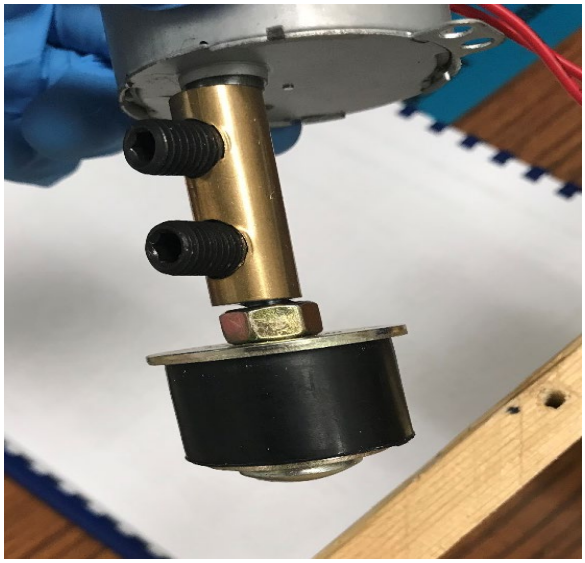

*Figure 4.17. Expansion plug attached to motor shaft.*

The rubber expansion plug was tightened in the PVC insert to connect it to the PVC insert (Figure 4.18).

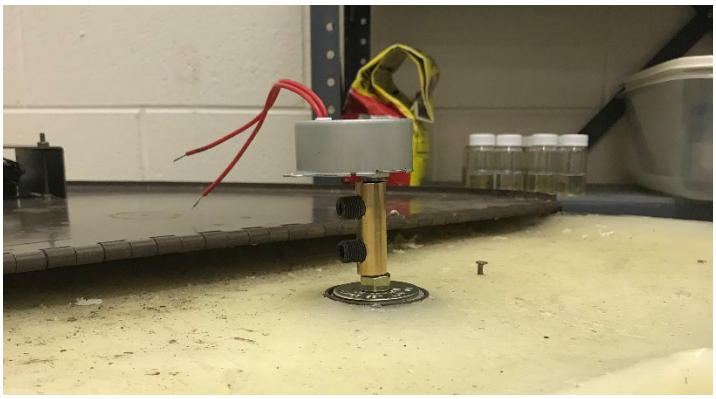

*Figure 4.18. CHANCS TYC-50 motor attached to the PVC insert.*

The motor was attached to a support structure made from two 64 cm long wooden boards, with dimensions of 3.6 cm x 1.5 cm. Two 15 cm long pieces with dimensions of 3.5 cm x 9.6 cm were cut and connected perpendicular to each side of the longer boards. The shorter pieces acted as anchors to attach the structure to the neutron howitzer's handles (Figure 4.19).

*Figure 4.19. Motor structure anchored into howitzer handles.*

The motor was wired to a switch, attached to the support structure which allowed it to be turned off when not in use (Figure 4.20).

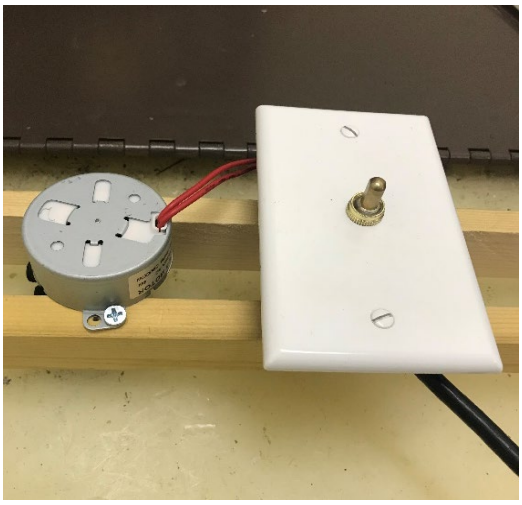

*Figure 4.20. Motor switch.*

Initial consistency tests showed that the motor did not significantly alter the isotropy of the system and therefore was removed. The results of initial consistency tests, including results of the ANOVA with and without the motor, are shown in Appendix B.

### *4.2.3 Neutron Activation Analysis of Indium Foils*

The four In foils used in this project were backed with aluminum for support. Direct measurements of the foil masses resulted in a total mass. The ratio of aluminum to In, and therefore the mass of In, was unknown. A NAA was performed to determine the mass of In in each foil. Using sleeve 2 and port 4, four Dy foils of known mass were irradiated 11.3 cm from the PuBe source with, and without, Cd covers. Eqn. 4.15 and Eqn. 2.1 were then used to determine the thermal neutron flux. The four In foils were irradiated with, and without, Cd covers using the same sleeve, port, and distance. The counts for each foil were used in Eqn. 4.17 to determine the mass of In present in the foil.

$$m = \frac{C_{net} \cdot W \cdot \lambda}{N_A \cdot \varphi \cdot \eta_F \cdot \eta_D \cdot \sigma \cdot (1 - e^{-\lambda t_1}) \cdot e^{-\lambda t_2} \cdot (1 - e^{-\lambda t_3})} \tag{4.17}$$

The irradiation, cooling, and counting times for each foil type are listed in Table 4.9.

*Table 4.9. Irradiation, cooling, and counting times for NAA of indium foils.*

| Foil Type | Irradiation Time [min] | Cooling Time [min] | Counting Time [min] |
|---|---|---|---|
| Dysprosium | 140 | 10 | 15 |
| Indium | 60 | 10 | 15 |

The results of the NAA are displayed in Appendix B.

## 4.3 THERMAL NEUTRON FLUX CHARACTERIZATION

Following NAA, the four In foils and four Dy foils were used to measure thermal neutron flux through the irradiation ports. Using the methods discussed in Section 4.1, bare foils and Cd covered foils were irradiated in each port using the foils and distances from the PuBe source listed in Table 4.10 and shown in Figure 4.21. Distances varied depending on the sleeve and spacers used; specific placement of foils and foil types was determined randomly (and was obviously dependent on the number of available foils).

*Table 4.10. Irradiation distances and foils used for each port.*

| Port | Distances [cm] | | | |
|---|---|---|---|---|
| 1 | 3.99(In), | 9.04(Dy), | 12.8(Dy), | 16.7(In) |
| 2 | 3.58(Dy), | 8.69(In), | 13.7(In) | |
| 3 | 3.58(In), | 9.04(In), | 13.7(Dy) | |
| 4 | 3.58(In), | 8.69(In), | 13.7(In) | |

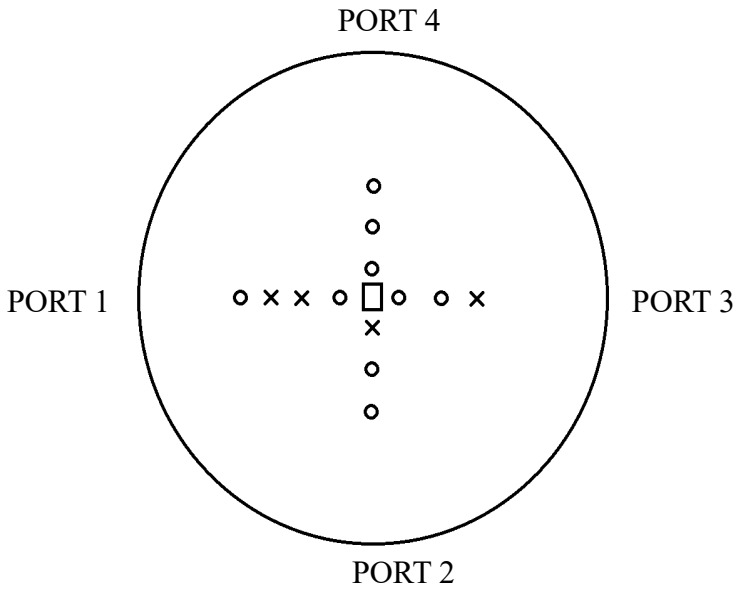


*Figure 4.21. Layout of measurements made for thermal neutron flux characterization.*

The $t_1$, $t_2$, and $t_3$ for each foil type are listed in Table 4.11. All times were recorded and any variations from the times in Table 4.11 were corrected for in Eqn. 4.15.

*Table 4.11. Irradiation, cooling, and counting times for In and Dy thermal foils.*

| Foil Type | Time [min] | | |
|---|---|---|---|
| | Irradiation ($t_1$) | Cooling ($t_2$) | Counting ($t_3$) |
| In | 108.5 | 15.5 | 15 |
| Dy | 280 | 15 | 15 |

The thermal neutron flux was calculated using Eqn. 2.1 for each distance within the ports. The *CR* was determined at each distance using Eqn. 2.2 to assess the level of thermalization that occurred within the ports.

## 4.4 MODELING THEORETICAL NEUTRON FLUX

MCNPX Version 2.7.0, produced by Los Alamos National Laboratory (LANL), was used to develop a theoretical model for neutron flux. MCNPX was chosen because it

can run multiple particle interactions and has cross-section databases necessary for neutron interactions. MCNP6 is also capable of running the simulations for this work, but there less information is available in the literature about its use. A general description of how the input code was written is presented in this section; refer to Appendix A for more detailed information.

The neutron howitzer was modeled within MCNPX as a series of vertical right circular cylinders (RCC) for the container and source port, and horizontal RCCs for the irradiation ports. The modeled barrel of the howitzer was filled with paraffin, the source port was filled with air, the irradiation ports were filled with PMMA. Another horizontal RCC was defined inside of the irradiation port and filled with the foil material (In or Dy). This foil "cell" (as termed in MCNP verbiage) was moved along the irradiation port to simulate different distances from the PuBe source.

A rectangular parallelepiped (RPP) was used to create the room surrounding the howitzer with a plane normal to the z-axis (PZ) for the floor. The room outside of the neutron howitzer and above the floor plane was filled with air and the room below the floor plane was filled with concrete. Everything outside of the room RPP was defined as void.

The PuBe source was represented by concentric RCCs. The inner cylinder was filled with the PuBe source active component ($PuBe_{13}$ ratio). The surrounding cylinder was filled with stainless steel. The source was defined as the active component (inner cylinder) and a sampling boundary was set tightly around it. Figure 4.22 shows a visual representation of the model.

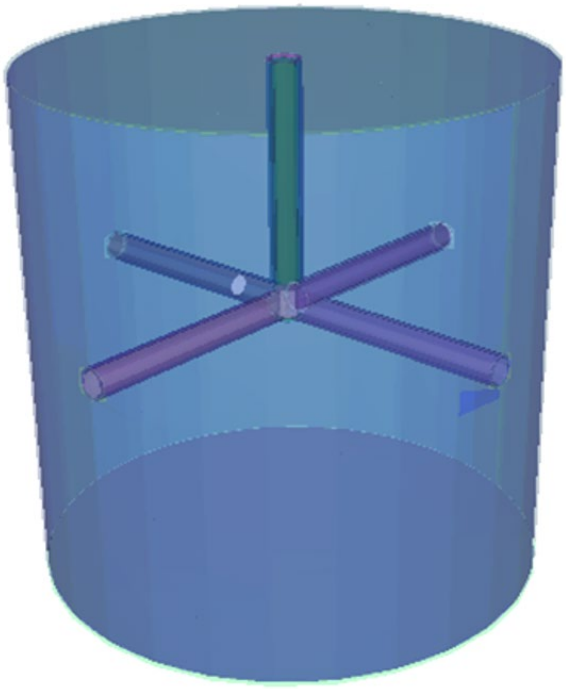

*Figure 4.22. MCNPX Visual Editor (VisedX version 24E) representation of the MCNPX flux code.*

Neutron energy spectra for $^{239}$PuBe alpha-neutron sources were created using version 4C of the SOURCES software (SOURCES-4C). Spectra were created using four compositions determined to be relevant from the literature, shown in Figure 4.23 [33-35].

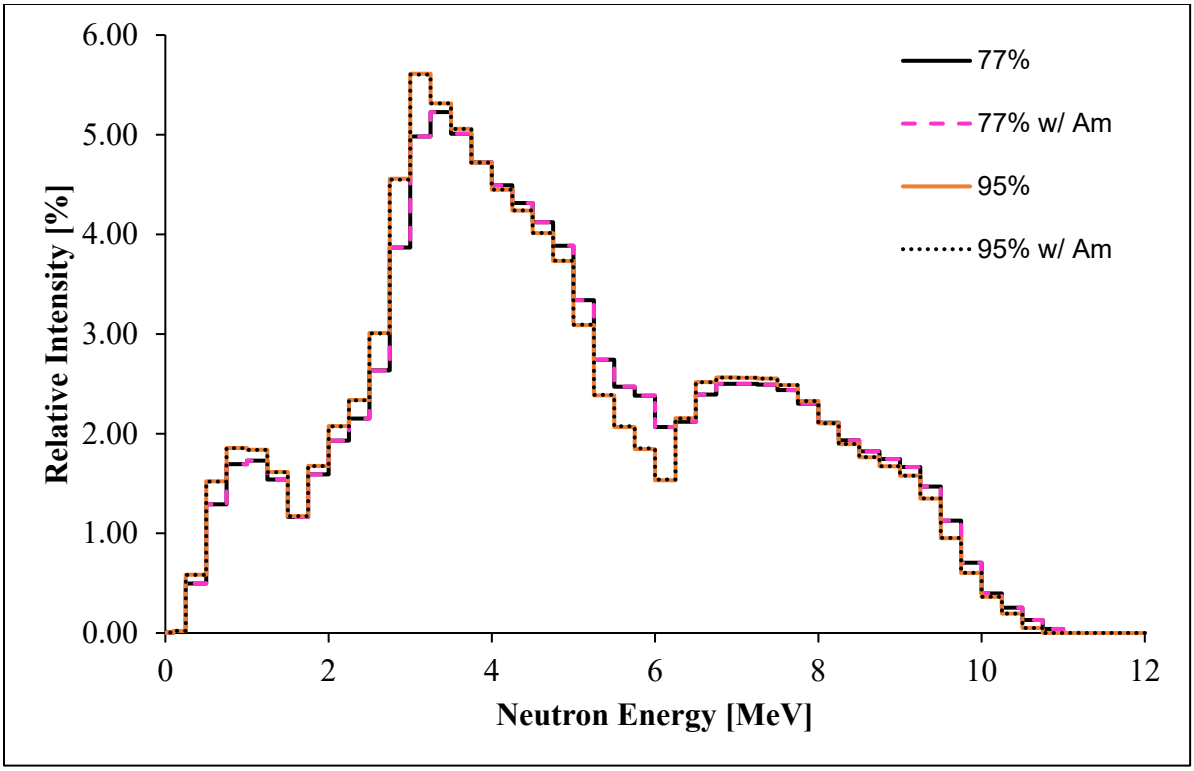


*Figure 4.23. $^{239}$PuBe neutron spectra for: (A) 77% $^{239}$Pu, (B) 95% $^{239}$Pu, (C) 77% $^{239}$Pu with $^{241}$Am contribution, and (D) 95% $^{239}$Pu with $^{241}$Am contribution.*

The spectra created using SOURCES-4C show that differences in the isotopic composition of the PuBe source does not significantly affect the energy distribution. The assumed isotopic composition from the $^{239}$PuBe alpha-neutron source used by Nguyen (2006) adequately modeled the energy spectrum of the PuBe source [35].

The F4 tally was used to determine the thermal neutron flux through the In foil. When the F4 tally is used, the MCNPX code calculates the neutron flux through a specified cell. Tallies can be organized by user-specified particle energies using the En card, where n is the tally number designation. Here, the E4 card was used with the F4 tally to calculate the neutron flux for energies up to 0.5 eV. The code was set to neutron (n) mode in the

source definition and $1x10^6$ particles were simulated using the nps (number of particles) card.

The output file reliability was evaluated based on the relative error and status of 10 standard statistical tests calculated automatically within MCNPX. Results with relative errors below 0.10 are reliable for all tallies except F5, which is considered reliable when the relative error is less than 0.05 [18]. If the relative error was too high to be considered reliable, or if the simulation didn't pass all the statistical tests, the number of particles was increased until the results passed both evaluations.

Output data from MCNPX codes are normalized and presented in output per source particle and must be multiplied by the source yield to get desired results. For example, the F4 tally output was in terms of neutrons $cm^{-2}$ per source particle and had to be multiplied by the yield (neutrons per second) determined by Eqn. 4.2 to yield neutrons $cm^{-2}$ $s^{-1}$. The corrected output from MCNPX was compared to the experimental data for thermal neutron flux to determine if the code accurately simulated the system. The neutron yield used to determine the theoretical thermal neutron flux (from MCNPX) was corrected using a correction factor (*CF*), determined by Eqn. 4.18.

$$CF = \frac{\varphi_{experimental}}{\varphi_{theoretical}} \tag{4.18}$$

The neutron yield needed correction because the original yield calculation assumed the PuBe source was only composed of $^{239}Pu$. The PuBe source composition likely contains $^{241}Am$ from the decay of $^{241}Pu$, which increases the neutron yield (discussed in Section

4.1.1). The corrected neutron yield was used for all following simulations to accurately model the system.

## 4.5 MODELING THEORETICAL NEUTRON DOSE

After verifying the MCNPX code using experimental thermal neutron flux data, it was adapted for dose modeling such that the output was $\dot{H}^*(10)$. A general description of the adjustments is provided in this section, but Appendix A provides more detailed information.

To mimic future bacterial irradiation experiments, the MCNP geometry was adjusted to represent cultured petri dishes within the irradiation ports. The PMMA material previously comprising the irradiation ports was replaced with air . The F4 tally was replaced with the F5 tally to give the neutron flux at a defined point, which is a more appropriate value for converting to dose. This "point detector" was moved along the irradiation port to simulate different distances from the PuBe source. The neutron flux was partitioned into energy bins and each bin was multiplied by the appropriate dose conversion factor (DCF) to get $\dot{H}^*(10)$ (ICRP 74) [26]. The $\dot{H}^*(10)$ corresponding to thermal neutron energies was converted to absorbed dose rate ($\dot{D}$) using the $Q$ value that corresponds to thermal neutron energies, which is 2.3.

Two RadEye detectors, RadEye™ NL Personal Neutron Meter ("RadEye NL" SN 10352) and RadEye™ B20 $\alpha\beta\gamma$ Survey Meter ("RadEye B20" SN 31893), were used to measure $\dot{H}^*(10)$ from neutron and gamma-ray radiation around the neutron howitzer. Thermo Scientific™ produced the RadEye NL and RadEye B20 detectors to alert users of

radiation exposures and to measure the radiation dose equivalent rates in an area or to a person. The RadEye detectors are shown in Figure 4.24.

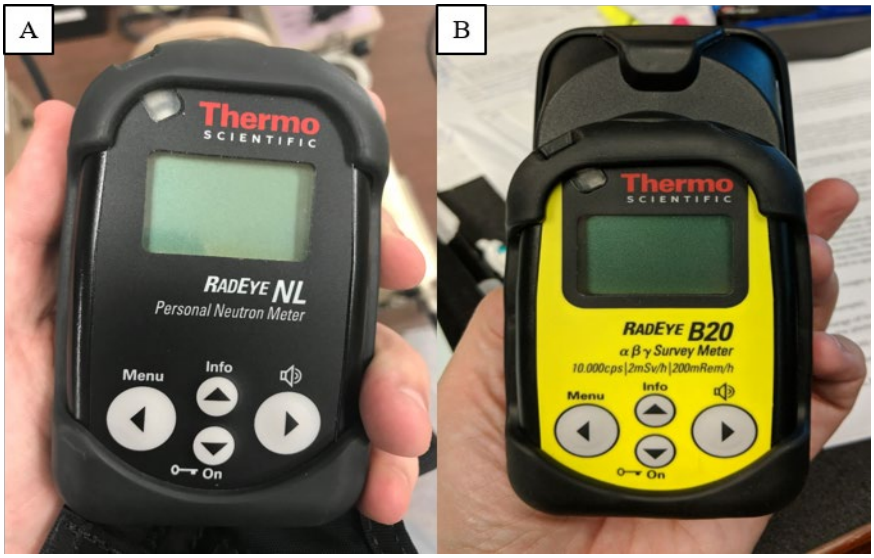


*Figure 4.24. (A) RadEye NL neutron detector and (B) RadEye B20 $\alpha\beta\gamma$ detector.*

## 4.6 UNCERTAINTY

Uncertainty was calculated using two methods for this work. For the preliminary consistency test, uncertainty was determined by one standard deviation of three trials. Eqn. 4.19 was used to calculate the standard deviation ($\sigma$).

$$\sigma = \sqrt{\frac{\sum_{i=1}^{n}(x_i - \bar{x})^2}{n-1}} \tag{4.19}$$

where, $n$ = number of data points
$x_i$ = value of data point $i$
$\bar{x}$ = mean of all $x_i$ values

For the NAA, thermal neutron flux characterization, and MCNPX data, uncertainty was determined using propagation of error. The general equation used for error propagation is given in Eqn. 4.20.

$$\sigma_u^2 = \left(\frac{\partial u}{\partial x}\right)^2 \sigma_x^2 + \left(\frac{\partial u}{\partial y}\right)^2 \sigma_y^2 + \left(\frac{\partial u}{\partial z}\right)^2 \sigma_z^2 + \ldots\ldots \quad (4.20)$$

For mass determination, Eqn. 4.21 was derived from Eqn. 4.20.

$$\sigma_m = \sqrt{\left(\frac{\sigma_{C_{net}}^2}{C_{net}^2}\right) + \left(\frac{\sigma_\varphi^2}{\varphi^2}\right) + \left(\frac{\sigma_{\eta_D}^2}{\eta_D^2}\right) + \left(\frac{\sigma_\sigma^2}{\sigma^2}\right)} \quad (4.21)$$

where, $\sigma_m$ = mass uncertainty

For neutron flux calculations, Eqn. 4.22 was derived from Eqn. 4.20.

$$\sigma_\varphi = \sqrt{\left(\frac{\sigma_{C_{net}}^2}{C_{net}^2}\right) + \left(\frac{\sigma_m^2}{m^2}\right) + \left(\frac{\sigma_{\eta_D}^2}{\eta_D^2}\right) + \left(\frac{\sigma_\sigma^2}{\sigma^2}\right)} \quad (4.22)$$

where, $\sigma_\varphi$ = neutron flux uncertainty

For MCNPX output data, Eqn. 4.23 was derived from Eqn. 4.20.

$$\sigma_{\varphi_{MCNP}} = \sqrt{\varphi_{MCNP}^2 \left[\left(\frac{\sigma_{X_{MCNP}}^2}{X_{MCNP}}\right) + \left(\frac{\sigma_Y^2}{Y^2}\right)\right]} \quad (4.23)$$

where, $\varphi_{MCNP}$ = neutron flux determined from MCNPX output
$X_{MCNP}$ = output data from MCNPX

CHAPTER FIVE

RESULTS AND DISCUSSION

## 5.1 THERMAL NEUTRON FLUX CHARACTERIZATION

As discussed above, bare and Cd neutron flux was measured to calculate thermal neutron flux at various distances from the PuBe source using Dy foil. The preliminary experiments showed that the neutron flux was generally independent of the port (see Section 4.2 and Appendix B) and therefore all data was plotted together (Figure 5.1). Different curves were fit to the data set with error bars represented by propagation of error associated with foil mass, cross-section data, counting statistics, and absolute detection efficiencies. Distances varied slightly due to differences in the sleeve construction.

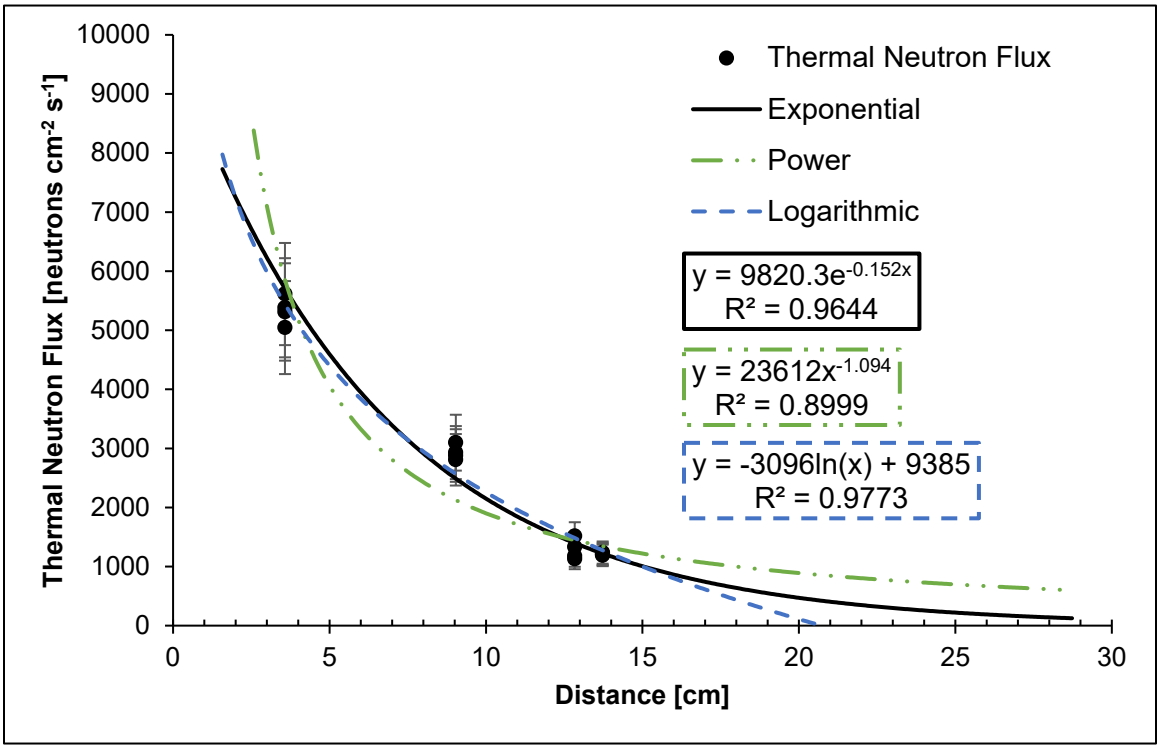


*Figure 5.1. Thermal neutron flux vs distance within the irradiation ports using Dy foil.*

The thermal neutron flux data was fit with three curves in Figure 5.1. The logarithmic curve reached the x-axis (i.e., 0 neutrons $cm^{-2}$ $s^{-1}$) around 21 cm, implying the thermal neutron field had been fully attenuated, while the exponential and power curves continued well beyond 30 cm. The exponential curve provides the most realistic model of the thermal neutron flux vs distance, which is expected for neutron attenuation [7].

Freeman (2010) measured the bare and Cd neutron flux at distances between 3 and 27 cm from the PuBe source using In foils [28]. The thermal neutron flux was calculated by finding the Cd difference (*CD*) using Eqn. 2.1 and was plotted against the experimental data of this work in Figure 5.2. The two data sets produce similar curves, confirming the hypothesis that the thermal neutron flux found in this work would agree with Freeman's results. Uncertainty was not given in the data provided by Freeman.

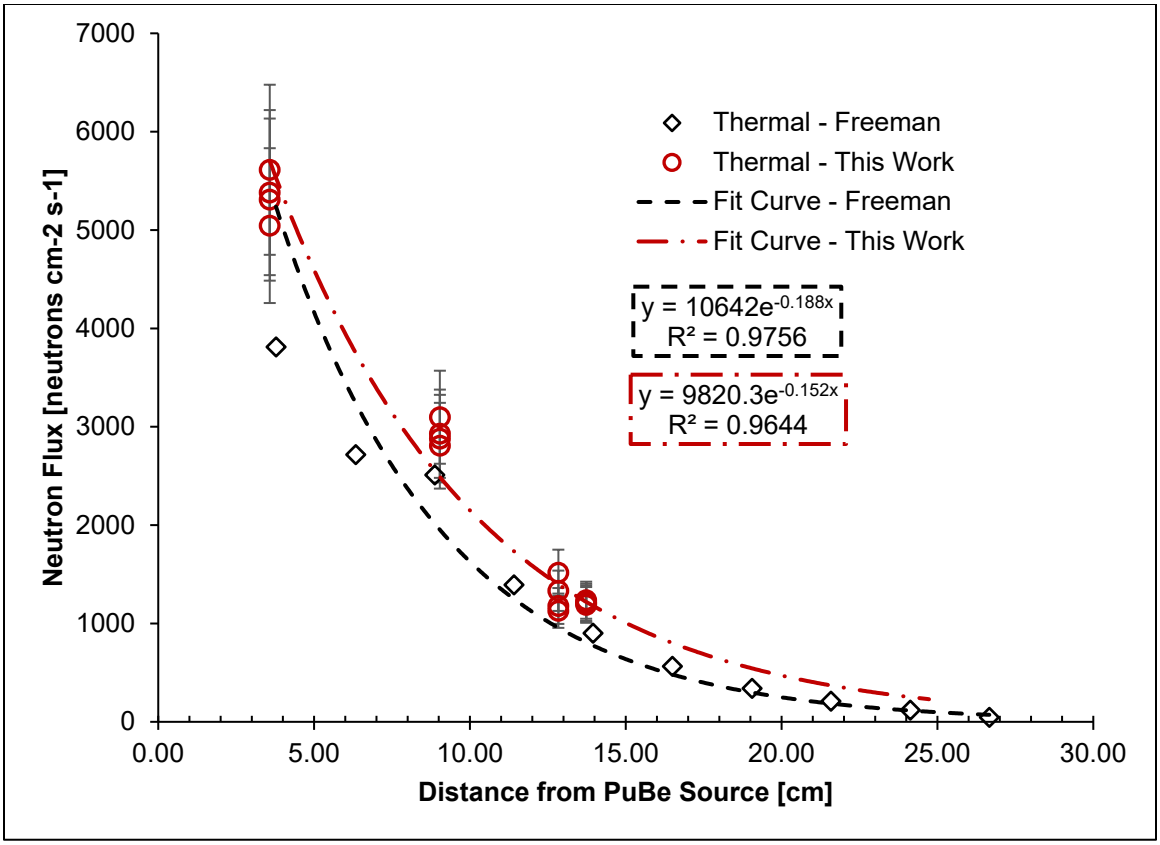


*Figure 5.2. Thermal neutron flux from Freeman (2010) (In foils) compared to this study (Dy foils).*

### *5.1.1 Cadmium Ratio*

The Cd ratio (*CR*) was determined for all distances using Eqn. 2.2 and presented in Table 5.1 for Dy foils, as well as In foils to show the different results that each foil type gave. Focus was placed on Dy foils for the remainder of this work because the masses of Dy foils could be accurately measured and therefore produced more reliable results.

*Table 5.1. Averaged Cd Ratios (CR) for all characterized distances and foil types.*

| Distance [cm] | Cadmium Ratio (*CR*) | |
|---|---|---|
| | Indium | Dysprosium |
| 3.58 | 5.58 ± 0.791 | 52.4 ± 11.2 |
| 3.99 | 4.97 ± 0.705 | - |
| 8.69 | 6.61 ± 0.940 | - |
| 9.04 | 6.82 ± 0.970 | 71.4 ± 15.3 |
| 12.8 | - | 68.3 ± 14.9 |
| 13.7 | 7.83 ± 1.13 | 85.8 ± 18.9 |
| 16.7 | 8.36 ± 1.21 | - |

*CR* was plotted against distance for In and Dy thermal foils in Figure 5.3.

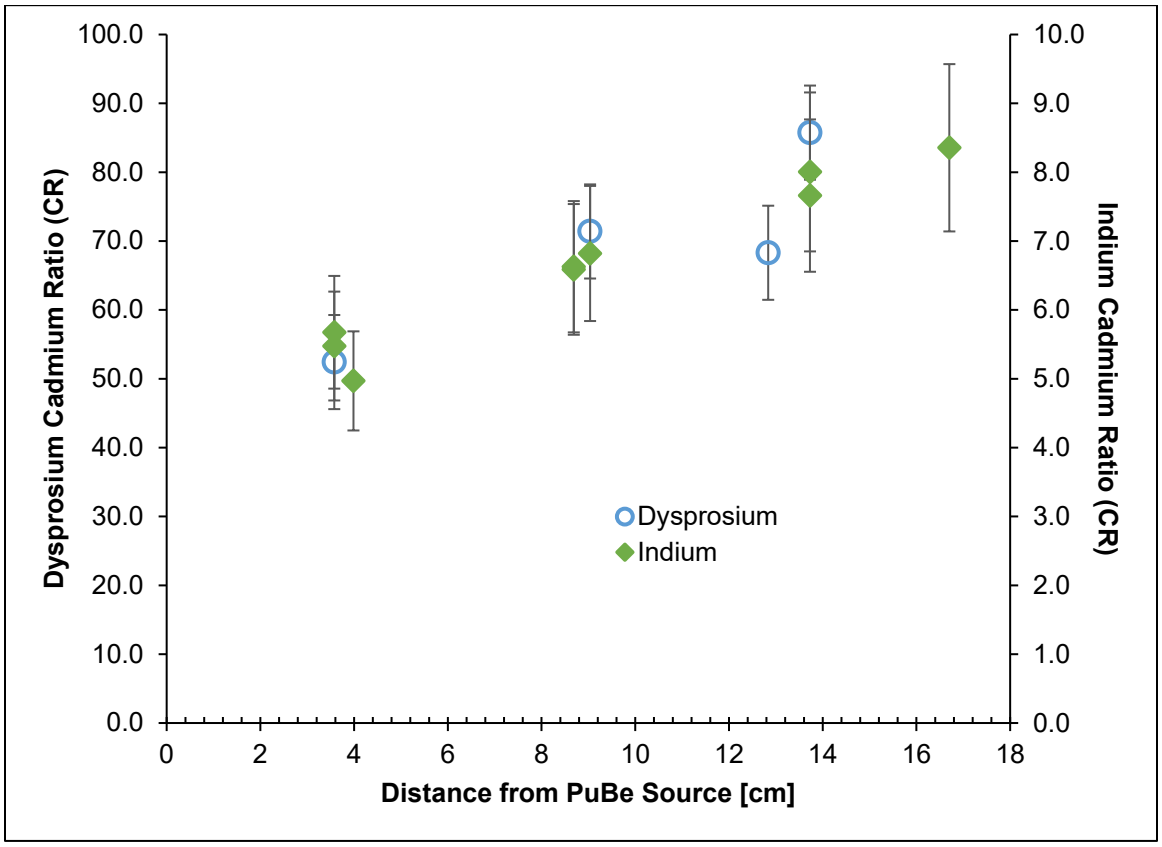


*Figure 5.3. Cd Ratios (CR) vs distance for indium and dysprosium thermal foils.*

The CR provides an indication of how thermalized a neutron field is, where higher CRs indicate a more thermalized neutron field. The CR is a function of moderation of the neutron field, which is a function of distance from the PuBe source, and was expected to

increase with distance as the neutron field was thermalized. This was confirmed by the experimental data presented in Figure 5.3. The *CR* is also dependent on the thermal foil used, as shown by Stuart and Ryan (1980) in their data of 69 radionuclides [45]. The differences are likely due to differences between resonance neutron cross-sections of various activation foils. Indium has a higher cross-section for neutron energies above 0.5 eV than Dy and therefore was activated by epithermal neutrons more than Dy, leading to lower *CR*s for In. For both In and Dy, the *CRs* follow an increasing trend from 52 to 86 for Dy and from 5.0 to 8.4 for In. Error bars represent propagated error from thermal neutron flux and Cd neutron flux in Eqn. 2.2. $F_{Cd}$ corrects the cadmium neutron flux for attenuation of epithermal neutrons in the Cd covers, while differences in *CR* are due to the variances in the capture cross-sections of each foil type. Therefore, the differences in *CR* are not accounted for by $F_{Cd}$.

## 5.2 MODELING THEORETICAL NEUTRON FLUX

The results of the F4 tally (flux averaged over a cell) are presented in Table 5.2 for the thermal neutron flux (0-0.5 eV) through an irradiation port filled with PMMA.

*Table 5.2. Thermal neutron flux (0-0.5 eV) determined by MCNPX simulation using the F4 tally.*

| Distance from Origin [cm] | Distance from Source [cm] | MCNPX Output [flux s neutron$^{-1}$] | Thermal Neutron Flux [neutrons cm$^{-2}$ s$^{-1}$] |
|---|---|---|---|
| 3.31 | 2 | $2.17\text{x}10^{-3} \pm 3.57\text{x}10^{-5}$ | $4536 \pm 250$ |
| 5.31 | 4 | $2.00\text{x}10^{-3} \pm 3.30\text{x}10^{-5}$ | $4188 \pm 231$ |
| 7.31 | 6 | $1.64\text{x}10^{-3} \pm 3.08\text{x}10^{-5}$ | $3434 \pm 192$ |
| 9.31 | 8 | $1.18\text{x}10^{-3} \pm 2.51\text{x}10^{-5}$ | $2469 \pm 140$ |
| 11.3 | 10 | $8.16\text{x}10^{-4} \pm 2.00\text{x}10^{-5}$ | $1708 \pm 99.1$ |
| 13.3 | 12 | $5.39\text{x}10^{-4} \pm 1.60\text{x}10^{-5}$ | $1129 \pm 68.2$ |
| 15.3 | 14 | $3.47\text{x}10^{-4} \pm 1.33\text{x}10^{-5}$ | $727.4 \pm 47.3$ |
| 17.3 | 16 | $2.18\text{x}10^{-4} \pm 9.53\text{x}10^{-6}$ | $455.5 \pm 31.2$ |
| 19.3 | 18 | $1.31\text{x}10^{-4} \pm 7.25\text{x}10^{-6}$ | $274.7 \pm 21.0$ |
| 21.3 | 20 | $8.81\text{x}10^{-5} \pm 6.06\text{x}10^{-6}$ | $184.5 \pm 16.0$ |
| 23.3 | 22 | $6.56\text{x}10^{-5} \pm 5.40\text{x}10^{-6}$ | $137.3 \pm 13.4$ |
| 25.3 | 24 | $3.30\text{x}10^{-5} \pm 3.48\text{x}10^{-6}$ | $69.11 \pm 8.14$ |
| 27.3 | 26 | $2.22\text{x}10^{-5} \pm 3.11\text{x}10^{-6}$ | $46.57 \pm 6.97$ |
| 29.3 | 28 | $6.45\text{x}10^{-6} \pm 1.49\text{x}10^{-6}$ | $13.50 \pm 3.20$ |

Distances in the first column represent the distance input into MCNPX, while the second column represents the distance from the source. The uncertainty associated with the MCNPX output was determined from uncertainty in the neutron yield and the relative error presented in the MCNPX output file. The thermal neutron flux was plotted vs distance in Figure 5.4.

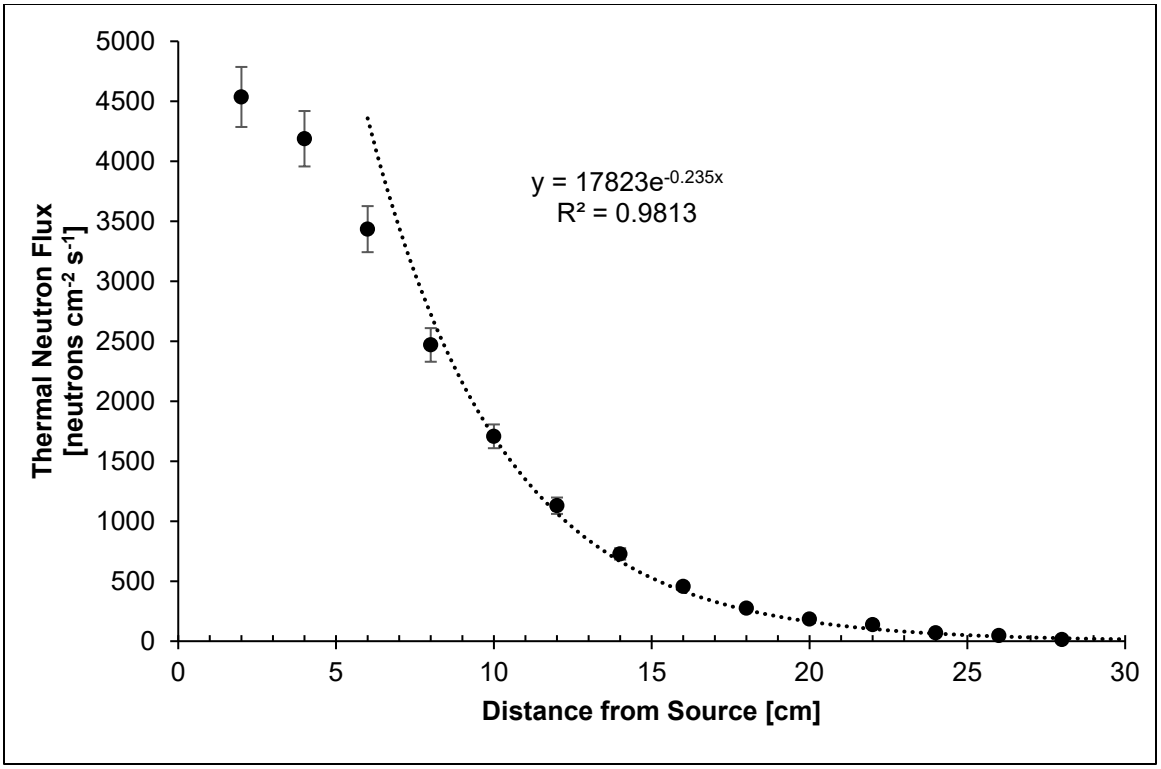


*Figure 5.4. Thermal neutron flux simulated with the F4 tally in MCNPX.*

An exponential curve was fit to the MCNPX data with an $R^2$ value of 0.9813, indicating the curve represents the data set well. Data points closer than 6 cm from the source clearly diverge from the exponential component and therefore were not included in the curve fit. The thermal neutron flux at the points closest to the source may have been lower than predicted by the curve because the neutron field had not been thermalized. Linear interpolation was utilized to determine flux between points at distances less than 6 cm from the source.

The impact of assuming the PuBe source isotopic composition and neutron spectra was assessed by rerunning the MCNPX code with a neutron spectrum from SOURCES-4C with a 95% $^{239}$Pu composition and a 0.7% $^{241}$Pu composition (decay corrected for 42 years

to get the $^{241}$Am composition). The thermal neutron flux data for each composition is compared in Figure 5.5.

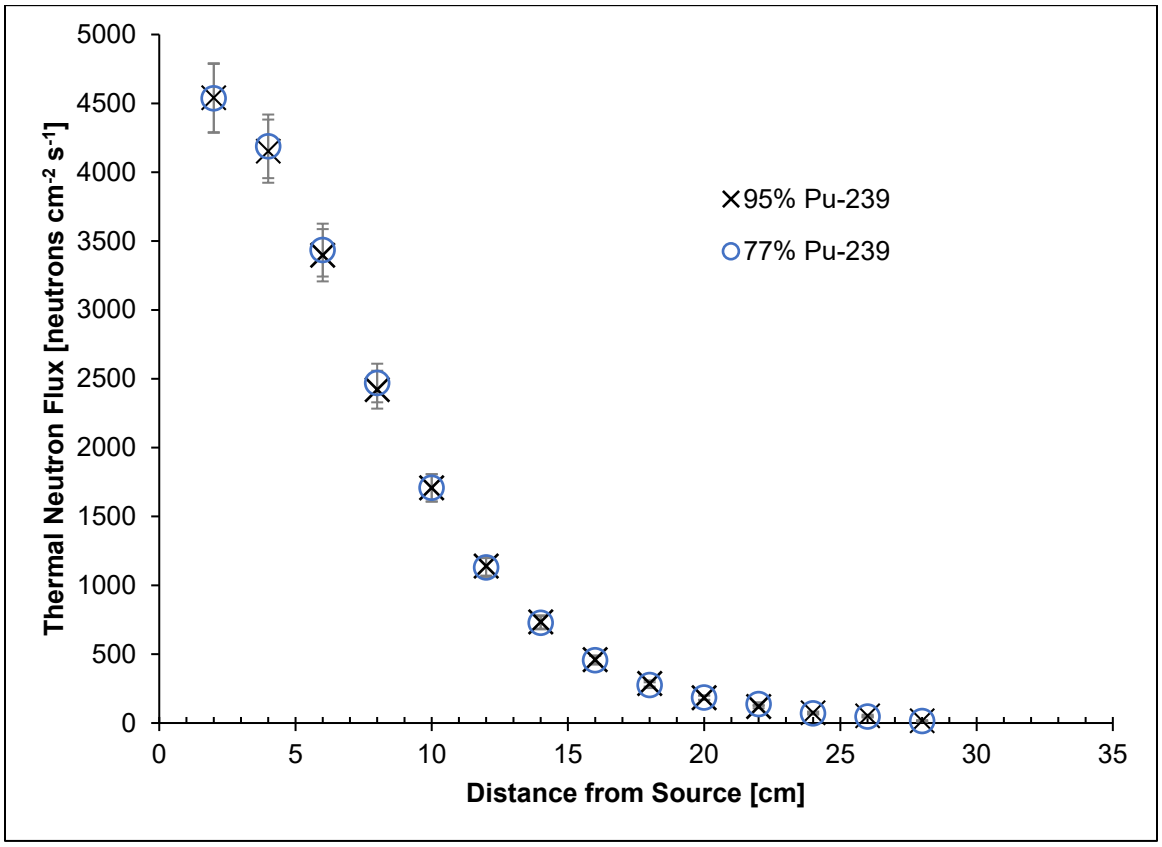


*Figure 5.5. Comparison of two PuBe source isotopic compositions: 77% $^{239}$Pu and 95% $^{239}$Pu.*

Note that the neutron yield was kept constant in the calculations that resulted in Figure 5.5. The data points in Figure 5.5 are nearly identical which reinforces the assumption that the neutron energy spectrum used for the MCNPX model did not significantly affect the thermal neutron flux. However, the neutron yield did have a large impact (Section 4.1.1); Figure 5.6 shows the MCNPX thermal neutron flux without a *CF* plotted with the experimental thermal neutron flux.

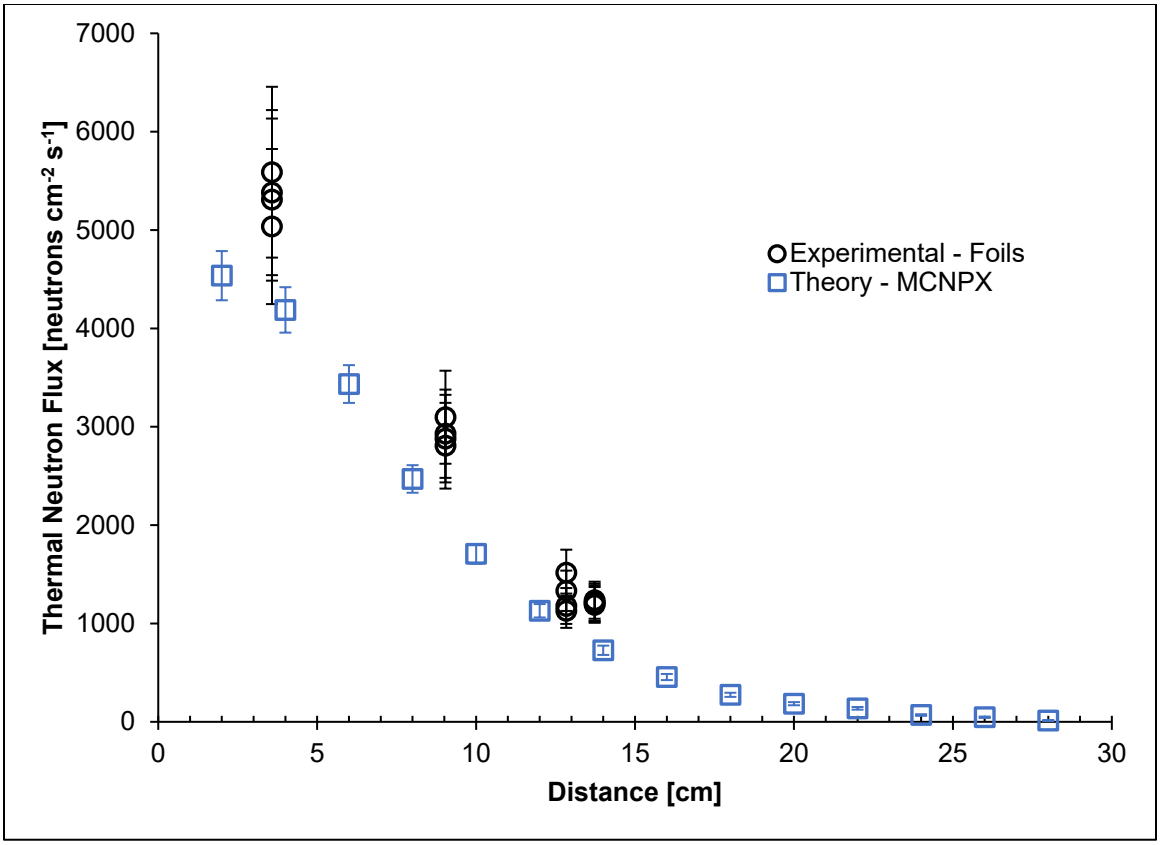


*Figure 5.6. Experimental thermal neutron flux plotted with MCNPX simulation data.*

Without confidently knowing the composition of the PuBe source, the neutron yield was estimated based on values from the literature. Therefore, a *CF* was determined to correct the MCNPX model output for flux, and then later for dose, based on experimental data. MCNP results were slightly lower than the experimental data, which is not unexpected as the neutron yield was expected to be an underestimation of the actual neutron yield. Table 5.3 shows the experimental and theoretical (MCNPX) data for thermal neutron flux along with the calculated correction factor for each distance measured.

*Table 5.3. Experimental verse theoretical thermal neutron flux data used to determine correction factors.*

| Distance From Source [cm] | Thermal Neutron Flux [neutron $cm^{-2}$ $s^{-1}$] | | Correction Factor (*CF*) |
|---|---|---|---|
| | Experimental | MCNPX[a] | |
| 3.577 | 5029 ± 745 | 4262 ± 280 | 1.18 ± 0.192 |
| 9.036 | 2619 ± 381 | 2132 ± 109 | 1.23 ± 0.189 |
| 12.837 | 1289 ± 199 | 872.7 ± 56.5 | 1.48 ± 0.247 |
| 13.729 | 1085 ± 150 | 707.6 ± 48.4 | 1.53 ± 0.237 |
| | | Average | 1.35 ± 0.216 |

[a]*Based on linear interpolation (distances < 6 cm) or exponential curve fit (distances > 6 cm)*

The average CF was determined and then used to correct the MCNPX model data. Adjusted thermal neutron flux data was then plotted in Figure 5.7 for verification.

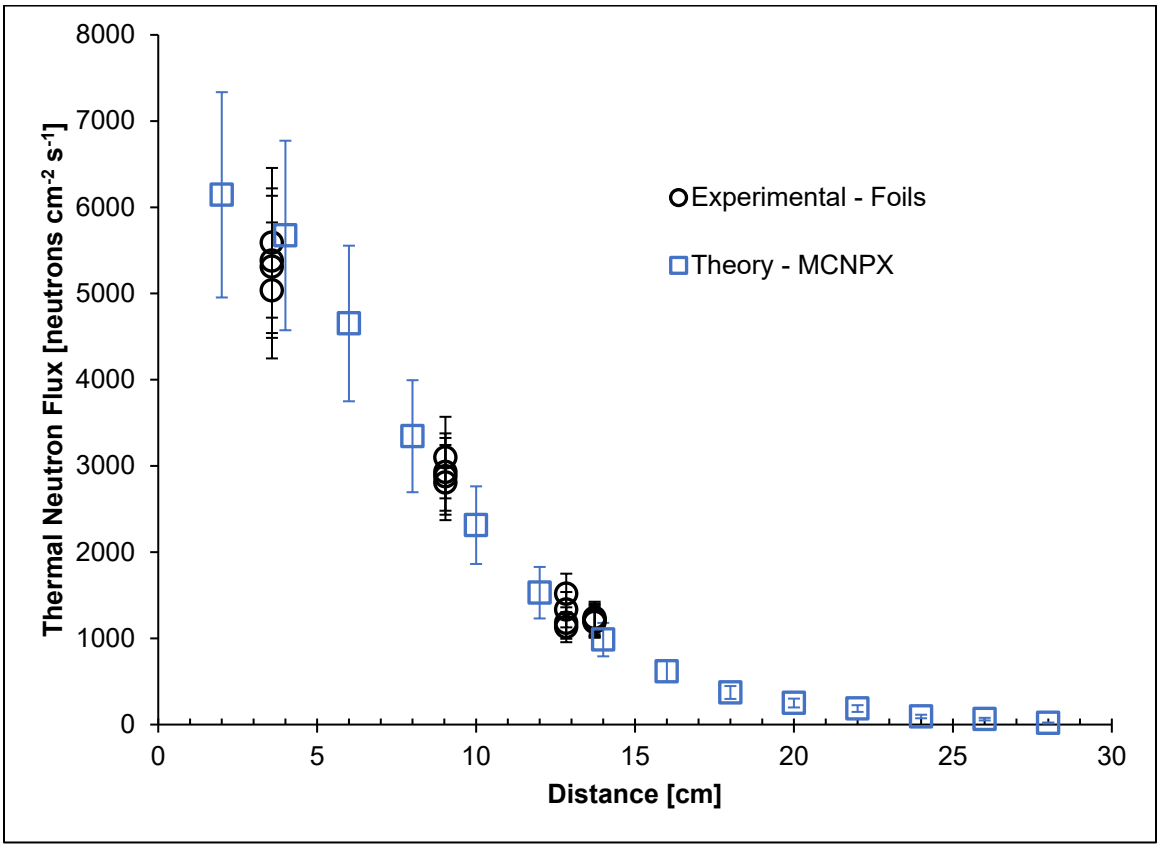


*Figure 5.7. Experimental verse theoretical thermal neutron flux with a CF of 1.35 ± 0.216.*

The model results fit the experimental data much better with the CF. This CF accounts for errors made in estimating the PuBe source composition, and therefore its neutron yield.

Relative neutron intensity was plotted against neutron energy in Figure 5.8 at a distance 1.7 cm from the PuBe source for comparison to Figure 2.2 and Figure 4.23.

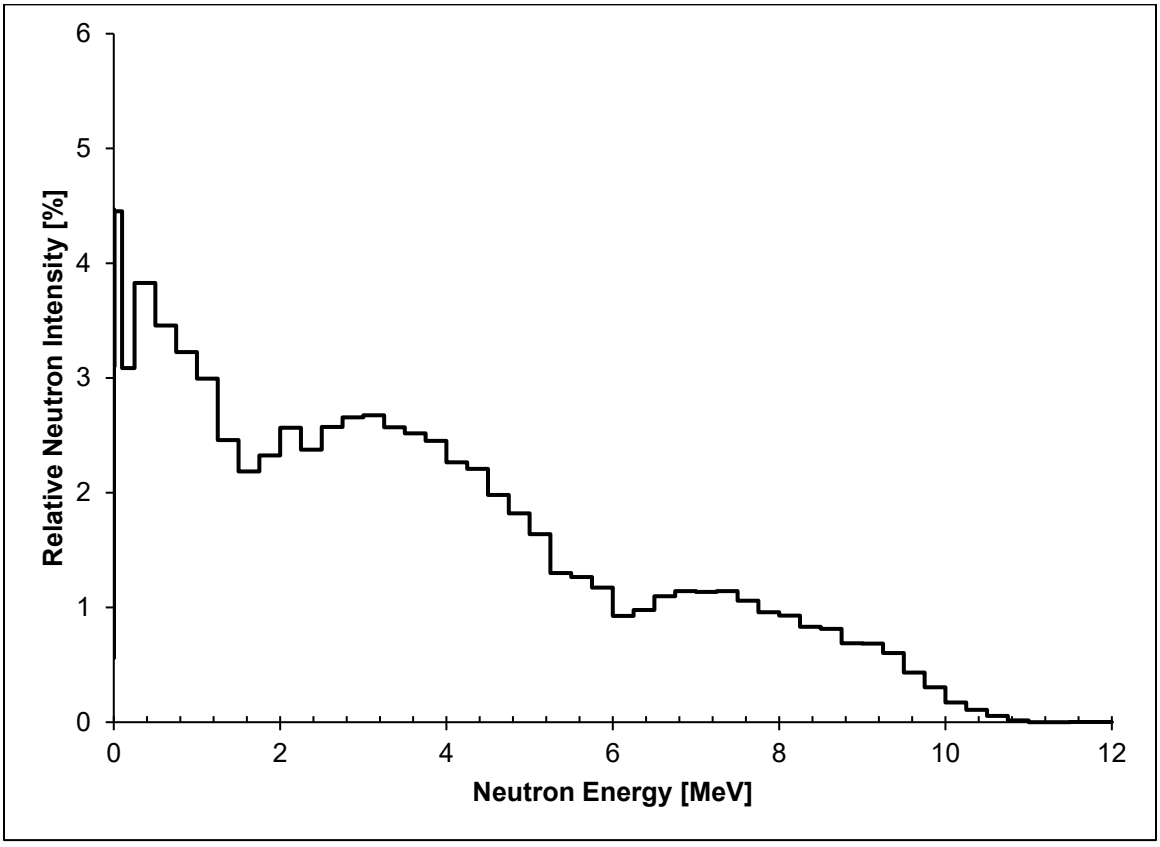


*Figure 5.8. Relative neutron intensity spectrum at a distance 1.7 cm from the PuBe source.*

The plotted spectrum in Figure 5.8 correlates well with the spectrum produced by Anderson (1972) in Figure 2.2, which showed a similar curve with dips around 1.75 and 6 MeV, peaks around 3 and 7 MeV, and a peak at low energies below 1 MeV. The SOURCES-4C spectrum in Figure 4.23 also showed the same shape and only differed at energies below 1 MeV, where SOURCES-4C did not predict a peak. SOURCES-4C simulated the neutron production of the PuBe source but does not simulate the neutron

interactions that occur inside the PuBe source itself. Neutrons interact with the PuBe material before they leave the PuBe source. The spectra in Figure 2.2 and 4.23 are representations of the neutron field immediately outside of the PuBe source.

The relative neutron energy spectra were also plotted for multiple distances from the PuBe source in Figure 5.9. In this plot, the neutron energy was plotted on the abscissa using a logarithmic scale which allowed the curve to be seen below 1 MeV (note that Figure 5.8 extends to 12 MeV).

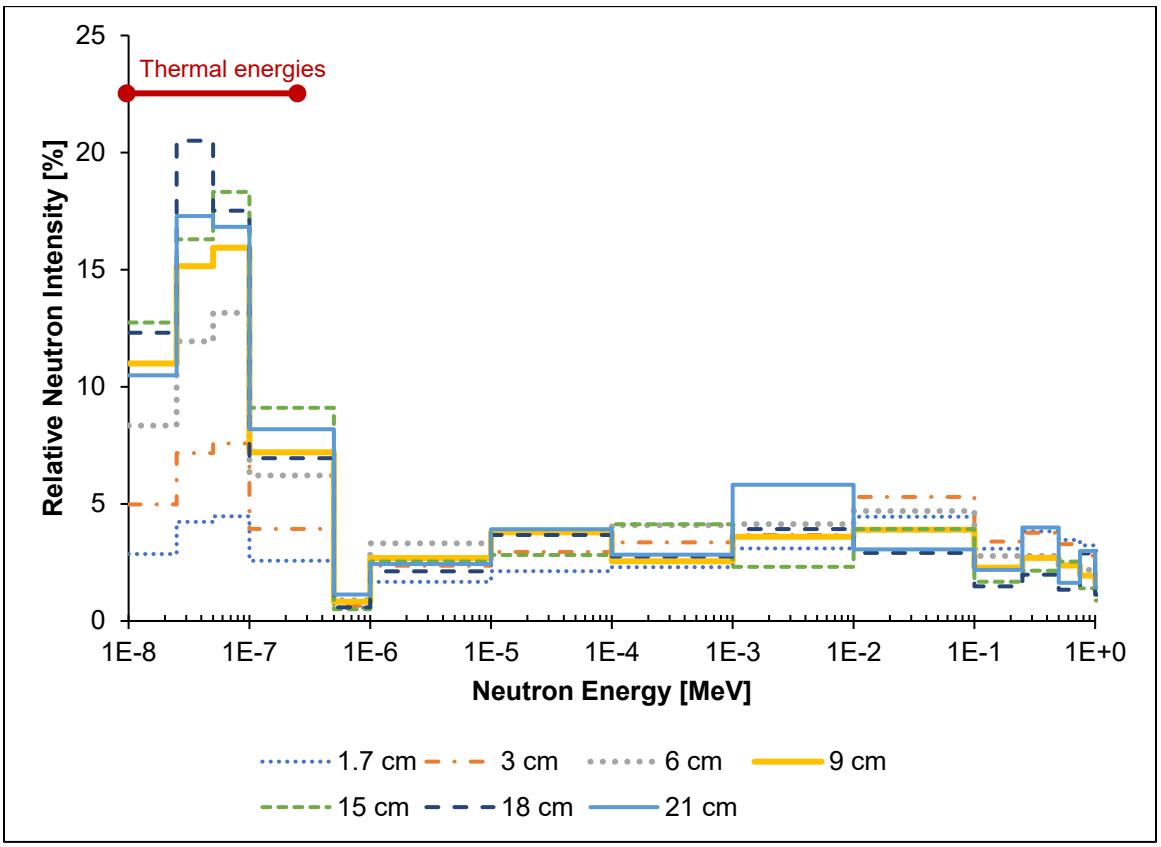


*Figure 5.9. Histogram of relative neutron intensity for various distances along the irradiation port.*

The level of thermalization that occurred can be seen clearly by the increasing peak at thermal energies (up to $5x10^{-7}$ MeV). The energy spectra were integrated from $2.5x10^{-8}$ to

$5x10^{-7}$ MeV to determine the percentage of the neutron flux that was thermalized, shown in Table 5.4.

*Table 5.4. Percentage of neutron flux with energies less than, or equal to, 0.5 eV.*

| Distance [cm] | Thermal Percentage [%] |
|---|---|
| 1.7 | 14.1 |
| 3.0 | 23.7 |
| 6.0 | 39.7 |
| 9.0 | 49.3 |
| 12 | 50.8 |
| 15 | 56.5 |
| 18 | 57.3 |
| 21 | 52.8 |

The cadmium ratio is an indicator to the level of thermalization that has occurred to a neutron field. Freeman (2010) found that the CR leveled out around 9 for In foils at distances greater than 15 cm from the PuBe source [28]. The CR in this work was also around 9 at 15 cm from the PuBe source for In foils, and it is assumed that it would have leveled off if there was more data (See Figure 5.3). The theoretical data in Table 5.4 shows that the percentage of the neutron field that was thermalized also leveled off around 15 cm.

## 5.3 MODELING THEORETICAL NEUTRON DOSE

The MCNPX flux code was adapted to produce $\dot{H}^*(10)$ by using the F5 tally and a dose conversion function utilizing ICRP 74 DCFs. The $\dot{H}^*(10)$ determined from MCNPX based on the corrected total neutron flux are presented in Table 5.5. Total $\dot{H}^*(10)$ ranged from 54.0 mrem $hr^{-1}$ (0.540 mSv $hr^{-1}$) to 3819 mrem $hr^{-1}$ (38.2 mSv $hr^{-1}$).

*Table 5.5. Total ambient dose equivalent rate determined using MCNPX tally F5 and DCFs.*

| Distance from Origin [cm] | Distance from PuBe Source [cm] | MCNP Output [mrem/hr per n/s] | Ambient Dose Equivalent Rate [mrem $hr^{-1}$] |
|---|---|---|---|
| 3.31 | 2 | $1.35\times10^{-3} \pm 1.88\times10^{-6}$ | 3819 ± 201 |
| 5.31 | 4 | $6.04\times10^{-4} \pm 8.46\times10^{-7}$ | 1717 ± 90.2 |
| 7.31 | 6 | $3.63\times10^{-4} \pm 5.08\times10^{-7}$ | 1030 ± 54.2 |
| 9.31 | 8 | $2.48\times10^{-4} \pm 4.46\times10^{-7}$ | 703 ± 37.0 |
| 11.3 | 10 | $1.79\times10^{-4} \pm 3.76\times10^{-7}$ | 508 ± 26.8 |
| 13.3 | 12 | $1.33\times10^{-4} \pm 3.32\times10^{-7}$ | 377 ± 19.9 |
| 15.3 | 14 | $1.01\times10^{-4} \pm 2.82\times10^{-7}$ | 286 ± 15.0 |
| 17.3 | 16 | $7.81\times10^{-5} \pm 2.50\times10^{-7}$ | 222 ± 11.7 |
| 19.3 | 18 | $6.13\times10^{-5} \pm 2.21\times10^{-7}$ | 174 ± 9.18 |
| 21.3 | 20 | $4.88\times10^{-5} \pm 1.91\times10^{-7}$ | 139 ± 7.31 |
| 23.3 | 22 | $3.94\times10^{-5} \pm 1.65\times10^{-7}$ | 112 ± 5.90 |
| 25.3 | 24 | $3.25\times10^{-5} \pm 1.46\times10^{-7}$ | 92.1 ± 4.86 |
| 27.3 | 26 | $2.68\times10^{-5} \pm 1.37\times10^{-7}$ | 76.0 ± 4.02 |
| 29.3 | 28 | $2.27\times10^{-5} \pm 1.18\times10^{-7}$ | 64.3 ± 3.40 |
| 31.3 | 30 | $1.90\times10^{-5} \pm 1.22\times10^{-7}$ | 54.0 ± 2.86 |

MCNPX also reported the $\dot{H}^{*}(10)$ due to the direct, or uncollided, neutron flux. The results of this output are presented in Table 5.6.

*Table 5.6. Direct (uncollided) ambient dose equivalent rate determined using MCNPX tally F5 and DCFs.*

| Distance from Origin [cm] | Distance from PuBe Source [cm] | MCNP Output [mrem/hr per n/s] | Ambient Dose Equivalent Rate [mrem $hr^{-1}$] |
|---|---|---|---|
| 3.31 | 2 | $7.55\times10^{-4} \pm 7.55\times10^{-7}$ | 2142 ± 113 |
| 5.31 | 4 | $2.95\times10^{-4} \pm 8.85\times10^{-8}$ | 837 ± 44.0 |
| 7.31 | 6 | $1.56\times10^{-4} \pm 3.11\times10^{-8}$ | 442 ± 23.2 |
| 9.31 | 8 | $9.60\times10^{-5} \pm 1.92\times10^{-8}$ | 272 ± 14.3 |
| 11.3 | 10 | $6.50\times10^{-5} \pm 1.30\times10^{-8}$ | 184 ± 9.70 |
| 13.3 | 12 | $4.69\times10^{-5} \pm 4.69\times10^{-9}$ | 133 ± 7.00 |
| 15.3 | 14 | $3.54\times10^{-5} \pm 3.54\times10^{-9}$ | 100 ± 5.29 |
| 17.3 | 16 | $2.77\times10^{-5} \pm 2.77\times10^{-9}$ | 78.6 ± 4.13 |
| 19.3 | 18 | $2.22\times10^{-5} \pm 2.22\times10^{-9}$ | 63.1 ± 3.32 |
| 21.3 | 20 | $1.83\times10^{-5} \pm 1.83\times10^{-9}$ | 51.8 ± 2.73 |
| 23.3 | 22 | $1.53\times10^{-5} \pm 1.53\times10^{-9}$ | 43.3 ± 2.28 |
| 25.3 | 24 | $1.29\times10^{-5} \pm 1.29\times10^{-9}$ | 36.7 ± 1.93 |
| 27.3 | 26 | $1.11\times10^{-5} \pm 1.11\times10^{-9}$ | 31.5 ± 1.66 |
| 29.3 | 28 | $9.64\times10^{-6} \pm 9.64\times10^{-10}$ | 27.3 ± 1.44 |
| 31.3 | 30 | $7.62\times10^{-6} \pm 7.62\times10^{-10}$ | 21.6 ± 1.14 |

Total $\dot{H}^*(10)$ considered all neutrons that reached the detector, while the direct $\dot{H}^*(10)$ considered only neutrons that had not undergone scattering interactions with other atoms or molecules [18]. The direct $\dot{H}^*(10)$ is not a measurable quantity in the experimental setup in this work because measurements made within the neutron howitzer cannot discriminate between neutrons that have, or have not, undergone scattering events. The simulated direct $\dot{H}^*(10)$ gives an idea of what the $\dot{H}^*(10)$ would be for the PuBe source without the neutron howitzer, which can be compared to the data from Shores (1999) [30].

The percentage of the $\dot{H}^*(10)$ that came from scattered neutrons are presented in Table 5.7.

*Table 5.7. Percentage of ambient dose equivalent rate from scattered neutrons.*

| Distance from PuBe Source [cm] | Scattered Neutron Contribution [%] | Distance from PuBe Source [cm] | Scattered Neutron Contribution [%] |
|---|---|---|---|
| 2 | 43.9 ± 3.3 | 16 | 64.5 ± 4.8 |
| 4 | 51.2 ± 3.8 | 18 | 63.7 ± 4.7 |
| 6 | 57.1 ± 4.3 | 20 | 62.6 ± 4.7 |
| 8 | 61.3 ± 4.6 | 22 | 61.3 ± 4.6 |
| 10 | 63.7 ± 4.7 | 24 | 60.2 ± 4.5 |
| 12 | 64.7 ± 4.8 | 26 | 58.5 ± 4.4 |
| 14 | 64.8 ± 4.8 | 28 | 57.5 ± 4.3 |

The contribution of the scattered neutron flux to the $\dot{H}^*(10)$ is greater than 50% for all distances greater than 2 cm from the PuBe source. A significant portion of the $\dot{H}^*(10)$ inside of the irradiation ports came from scattered neutrons. Therefore, the $\dot{H}^*(10)$ inside of the irradiation ports was significantly higher than the $\dot{H}^*(10)$ measured at an equal

distance with the PuBe source removed from the neutron howitzer. Total $\dot{H}^*(10)$ provides a more accurate measure of the $\dot{H}^*(10)$ bacterial samples will be exposed to.

$\dot{H}^*(10)$ are plotted in Figure 5.10 for the total and direct (uncollided) neutron dose through the irradiation ports with the PuBe source in the neutron howitzer. For comparison, the curve for DDE from Shores (1999) data was included in the figure for an unmoderated source [30].

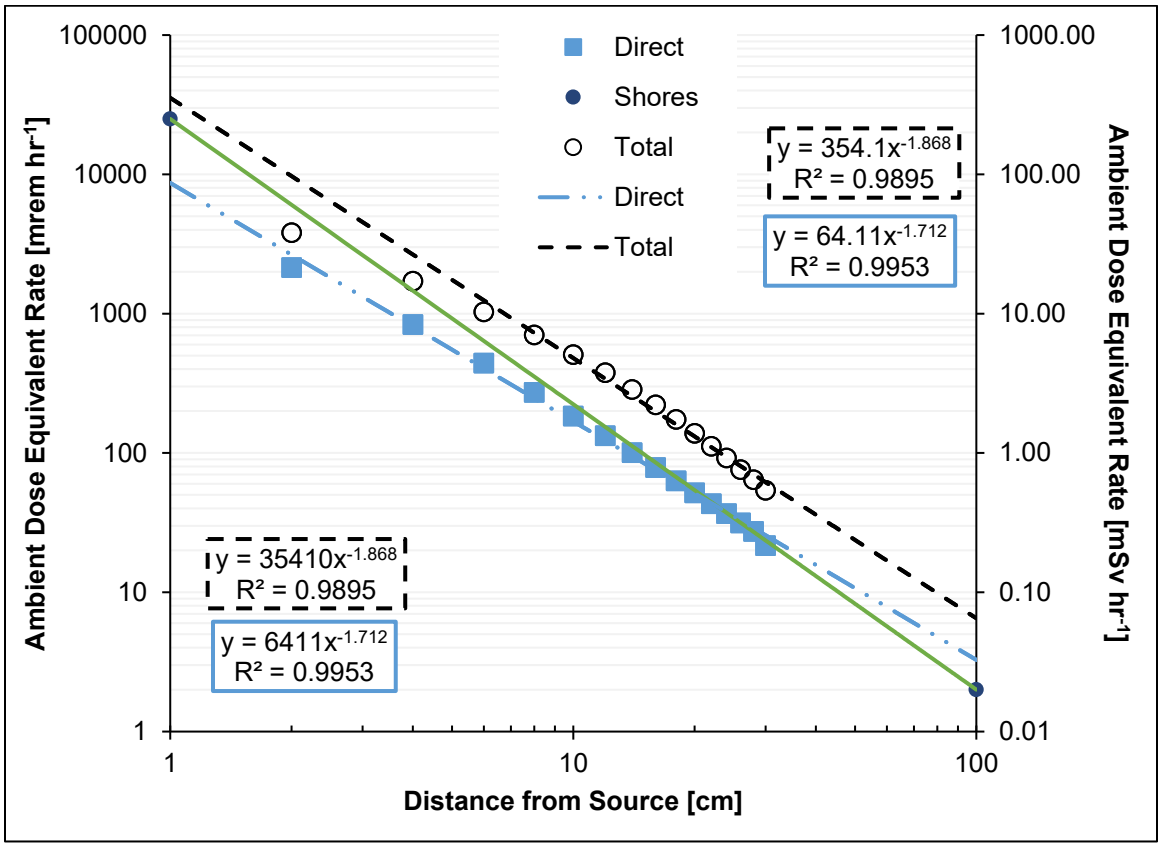


*Figure 5.10. Ambient dose equivalent rate plotted against distance from PuBe source.*

The conversion from neutron flux to $\dot{H}^*(10)$ requires splitting the neutron flux into multiple energy bins and multiplying by energy dependent DCFs. Therefore, the conversion is not a one-to-one calculation, which leads to a curve that is not exponential

like the one for thermal neutron flux (Figure 5.1). The theoretical direct $\dot{H}^*(10)$ from the MCNPX code follows the data produced by Shores very well at distances above 10 cm from the PuBe source.

Measurements were made at different locations around the neutron howitzer with the RadEye$^{TM}$ NL neutron detector and RadEye$^{TM}$ B20 $\alpha\beta\gamma$ detector and are shown in Table 5.8.

*Table 5.8. RadEye$^{TM}$ NL and RadEye$^{TM}$ B20 measurements of ambient dose equivalent rate at different locations.*

| Location | Ambient Dose Equivalent Rate [mrem hr$^{-1}$] | |
|---|---|---|
| | RadEye$^{TM}$ NL | RadEye$^{TM}$ B20 |
| Background | 0.12 | 0.025 |
| End of irradiation port (PMMA)[a] | 4.4 | 1.0 |
| End of irradiation port (air)[b] | 18 | 3.5 |
| 31 cm from PuBe source[c] | 5.7 | 1.0 |

[a] *Measured at the end of the irradiation port (approximately 31 cm) with the PMMA sleeve loaded.*
[b] *Measured at the end of the irradiation port with the PMMA sleeve removed.*
[c] *Source removed from howitzer and measured at distance equal to irradiation port length.*

Considering the RadEye$^{TM}$ NL detector, the measured $\dot{H}^*(10)$ at ~31 cm from the PuBe source was 18 mrem hr$^{-1}$ when measured through the irradiation port without a sleeve loaded and was 5.7 mrem hr$^{-1}$ when the PuBe source was measured ~31 cm away, outside of the neutron howitzer. To perform the measurements outside of the neutron howitzer, the RadEye$^{TM}$ NL detector was held at the top outer edge of the neutron howitzer (~31 cm from the source port), and the PuBe source was lifted out of the source port just long enough to record a dose rate before being placed back inside the center of the neutron howitzer. The measurement was performed in this way to keep exposure as low as reasonably

achievable (ALARA) and was considered a rough measurement used as a "common sense" check of the MCNPX dose rates [25]. It is assumed that this dose rate also considered scattered neutrons off the top of the neutron howitzer. Measurements made with the detector do not discriminate between scattered and uncollided neutrons, and therefore are analogous to the total $\dot{H}^*(10)$. The $\dot{H}^*(10)$ measured with the RadEye$^{TM}$ detector at the end of the howitzer port was within an order of magnitude of the total $\dot{H}^*(10)$ calculated by the MCNPX code. Although the RadEye$^{TM}$ detector needed calibration, which likely explains the differences between the detector and the theoretical output from MCNPX, it provided a verification of the MCNPX model accuracy. Considering the other measurements made, the RadEye$^{TM}$ B20 measurement at the end of the irradiation port through air shows an $\dot{H}^*(10)$ of 3.5 mrem hr$^{-1}$ due to gamma-rays.

The desired $\dot{D}$ in future bacterial irradiation experiment is about 10 mGy d$^{-1}$. The determined $\dot{H}^*(10)$ for the PuBe source were converted to $\dot{D}$ using the thermal neutron quality factor, 2.3, as a best estimate. At distances from the PuBe source greater than 10 cm, thermal neutrons made up the majority of the neutron field. The calculated $\dot{D}$s are displayed in Table 5.9 and Figure 5.11, along with the corresponding $\dot{H}^*(10)$ values.

*Table 5.9. Ambient dose equivalent rate and absorbed dose rates through the irradiation ports.*

| Distance from PuBe Source [cm] | Ambient Dose Equivalent Rate [mrem $hr^{-1}$] | Estimated Absorbed Dose Rate [mGy $d^{-1}$] |
|---|---|---|
| 2 | 3819 ± 201 | 398 ± 21 |
| 4 | 1714 ± 90.2 | 179 ± 9.4 |
| 6 | 1030 ± 54.2 | 107 ± 5.7 |
| 8 | 703 ± 37.0 | 73.4 ± 3.9 |
| 10 | 508 ± 26.8 | 53.0 ± 2.8 |
| 12 | 377 ± 19.9 | 39.3 ± 2.1 |
| 14 | 286 ± 15.0 | 29.8 ± 1.6 |
| 16 | 222 ± 11.7 | 23.1 ± 1.2 |
| 18 | 174 ± 9.18 | 18.2 ± 0.96 |
| 20 | 139 ± 7.31 | 14.5 ± 0.76 |
| 22 | 112 ± 5.90 | 11.7 ± 0.62 |
| 24 | 92.1 ± 4.86 | 9.61 ± 0.51 |
| 26 | 76.0 ± 4.02 | 7.93 ± 0.42 |
| 28 | 64.3 ± 3.40 | 6.71 ± 0.35 |
| 30 | 54.0 ± 2.86 | 5.63 ± 0.30 |

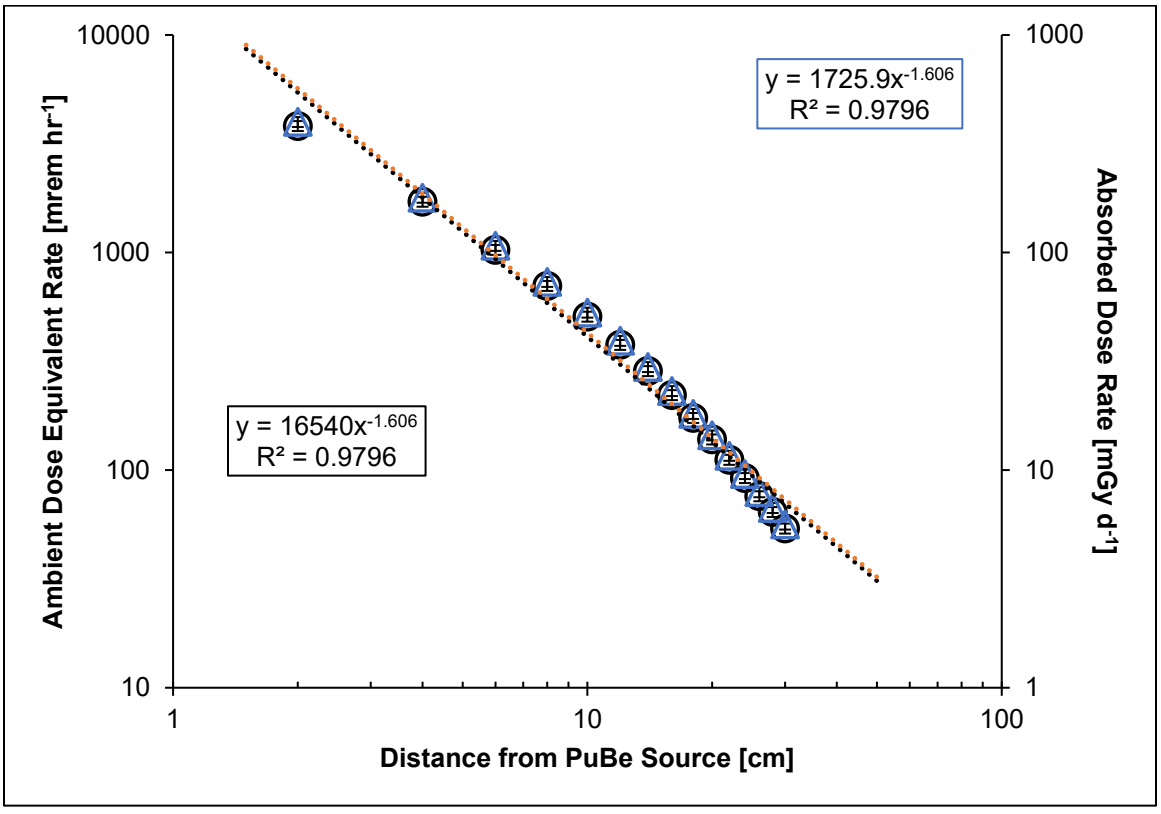


*Figure 5.11. Total ambient dose equivalent rate and absorbed dose rates produced by MCNPX.*

# CHAPTER SIX
# CONCLUSION AND FUTURE WORK

## 6.1 CONCLUSION

Thermal neutron flux of the PuBe source was characterized using Dy activation foils. Findings from this work agreed well with data produced by Freeman (2010) on the same PuBe source [28]. This work provided a more robust characterization of the thermal neutron flux and is expected to be a more accurate representation of the PuBe source.

The MCNPX code written to simulate the system was verified by the experimental thermal neutron flux. The thermal neutron flux provided an adequate means to verify the MCNPX code as evidenced by the relative neutron spectra in Figure 5.9 and Table 5.4. At distances within the irradiation ports greater than 10 cm from the PuBe source, the thermal neutron field represents over half of the total neutron field. A major source of uncertainty in this work was associated with assumptions made in the PuBe source definition. Differences in the PuBe source composition had little effect on the neutron energy distribution (Figure 4.23). The major differences between PuBe source compositions was the percentages of $^{239}$Pu, $^{240}$Pu, and $^{241}$Pu. The average alpha energy of $^{239}$Pu (5.15 MeV) and $^{240}$Pu (5.16 MeV) are about the same and therefore produce similar energy neutrons. $^{241}$Pu decays to $^{241}$Am, which has an average alpha energy (5.49 MeV) significantly higher than $^{239}$Pu and $^{240}$Pu [42]. The contribution of $^{241}$Am in the neutron yield was corrected for by the use of a CF equal to 1.35. The resulting MCNPX code produced $\dot{H}^{*}(10)$ through

the irradiation ports that followed expectations based on Shores (1999) as indicated in Figure 5.10 [38].

A $\dot{D}$ of 10 mGy $d^{-1}$ was desired for irradiation of bacterial samples. Interpolating between the $\dot{D}$'s at 22 and 24 cm from the PuBe source, it was determined that a $\dot{D}$ of 10 mGy $d^{-1}$ could be achieved at a distance of 23.6 cm from the PuBe source. The $\dot{D}$ estimates were based on a simplified estimation to convert $\dot{H}^{*}(10)$ to $\dot{D}$ based on the thermal neutron $Q$-value of 2.3. This method provided a reasonably accurate dose determination as required for bacterial irradiations.

The findings of this work also have impacts unrelated to the main objectives. The characterization provided for the PuBe source in this work can be used to calibrate various detection equipment including TLDs, Bonner spheres, Radeye$^{TM}$ detectors, and others. In addition to calibration, the dose characterization of the PuBe source opens the door to many other neutron dose-response experiments.

## 6.2 FUTURE WORK

The MCNPX code fidelity could be improved through an accurate measurement (or confirmation) of the PuBe source composition and energy spectrum. A gamma-spectroscopy analysis of the PuBe source would provide a means for determining the composition of Pu and Am radioisotopes in the source. Nguyen (2006) measured $^{239}$PuBe alpha-neutron compositions using a non-destructive, gamma-spectrometric method. Nguyen (2006) determined isotopic compositions of eight $^{239}$PuBe alpha-neutron sources, including the source used to estimate the composition in this work [35]. This method could

be performed on the PuBe source to create an accurate neutron energy spectrum that would improve the accuracy of the MCNPX code.

The goal of the overall project encompassing this work is to determine the discriminatory effects of specific radiation types. Measurements made with the RadEye$^{TM}$ B20 detector confirmed a measurable gamma-ray dose rate from the PuBe source. Therefore, it is important to address the gamma-ray emissions from the PuBe source. The gamma-ray energies and intensities produced by the PuBe source can be estimated using the composition of $^{239}$Pu and $^{241}$Am, where the $^{241}$Am composition could be determined by the increase in neutron yield indicated by the CF of 1.35 ± 0.216. Using this information about the gamma-ray emissions of the PuBe source, the MCNPX code could be adapted to quantify the $\dot{H}^{*}(10)$ due to gamma-rays produced by the PuBe source as well as from recoil gamma-rays, prompt gamma-rays, and other gamma-ray sources. If the dose from gamma-rays is significant, future researchers may consider using a lead plug between the bacterial samples and PuBe source to eliminate the gamma-ray contribution. This can be easily added in the MCNPX code to determine the effect it will have on the gamma-ray dose rate, as well as the neutron dose rate.

# APPENDICES

# APPENDIX A

The MCNPX flux code is included in Appendix A.1 to show how the code was written. Comments have been added to aid in the understanding of the code. The sections of code that were adjusted between the MCNPX flux code and the MCNPX dose code were outlined and numbered in red. The changes are shown in Appendix A.2.

# APPENDIX A.1 – MCNPX FLUX CODE

```
c ------------------------------------------------------------------------------
c
c THERMAL NEUTRON FLUX THROUGH IRRADIATION PORT
c
c ------------------------------ CELL CARDS ------------------------------------
c ------------------------------------------------------------------------------
c
c   Cell cards follow the form:
c   Designator   Material   Density   Location   Details   $ Comments
c
c ------------------------------------------------------------------------------
c ---------- HOWITZER ------------------
c
c Example: The outer barrel of the neutron howitzer is designated as cell 50, is
c filled with material 4 with a density of 8.00 g cm-3, is inside of surface 1
c and outside of surfaces 2 and 5, has a neutron importance of 1, and is
c commented as the outer barrel.
c
50  4  -8.00      -1   2   5             imp:n=1 $ outer barrel
51  1  -0.930     -2   5   8    10 12 14 imp:n=1 $ inner barrel
C ---------- SOURCE PORT ---------------
52  3  -0.001205  -1   2  -6             imp:n=1 $ air entry
53  4  -8.00      -5   6   2 -1          imp:n=1 $ steel entry
54  4  -8.00      -5   6   8 -2 10 12 14 imp:n=1 $ steel source port
55  3  -0.001205  -7  -2   16            imp:n=1 $ air source port
56  2  -1.406      7  -6  -2             imp:n=1 $ PVC
c ---------- IRRADIATION PORTS ---------
60  4  -8.00      -8   9   6 -2          imp:n=1 $ Port 1 - outer steel
61  6  -1.18      -9   6  -2             imp:n=1 $ Port 1 - inner PMMA
62  4  -8.00      -10  11  6 -2  12      imp:n=1 $ Port 2 - outer steel
63  6  -1.18      -11  6  -2  17         imp:n=1 $ Port 2 - inner PMMA
64  4  -8.00      -12  13  6 -2  8       imp:n=1 $ Port 3 - outer steel
65  6  -1.18      -13  6  -2             imp:n=1 $ Port 3 - inner PMMA
66  4  -8.00      -14  15  6 -2  8 10    imp:n=1 $ Port 4 - outer steel
67  6  -1.18      -15  6  -2             imp:n=1 $ Port 4 - inner PMMA
c ---------- PUBE SOURCE ---------------
70  7  -2.918     -18                   imp:n=1 $ PuBe Material
71  4  -8.00      -16  18               imp:n=1 $ Steel Encasing
c ---------- FOIL (In) -----------------
80  8  -7.31      -17                   imp:n=1 $ Indium
c ---------- SURROUNDINGS --------------
90  3  -0.001205   1   3  -4            imp:n=1 $ air in room
91  5  -2.30      -3  -4                imp:n=1 $ concrete floor
c ---------- Universe (void) -----------
100 0              4   3                imp:n=0
101 0              4  -3                imp:n=0

c ------------------------------------------------------------------------------
c ---------------------------- SURFACE CARDS -----------------------------------
c
c   Surface cards follow the form:
c   Designator   Shape   Shape Definition   $ Comments
c
c ------------------------------------------------------------------------------
c ---------- BARRELL -------------------
c -------------------------------------
c  RCC = Right Circular Cylinder
c        x  y  z  (base)      x  y  z  (extension)   radius
1  RCC   0  0  -30.48         0  0  60.96            30.5595   $ Outer barrel
2  RCC   0  0  -30.138        0  0  60.276           30.2175   $ Inner barrel
c  PZ = plane normal to the z-axis
c       z-coordinate
3  PZ   -30.48001                                             $ Floor
c  RPP = Rectangular Parallelepiped
```

1

```
c         x_min  x_max     y_min  y_max     z_min  z_max
4  RPP    -200   200       -200   200       -200   200           $ Room
c 4 RPP   -1.32  1.32      -1.32  1.32      -0.02  3.33 $ Test sampling boundary
c ---------- SOURCE PORT ---------------
5  RCC    0  0  -0.3125        0  0  30.7925          2.06
6  RCC    0  0  -0.3125        0  0  30.7925          1.718
7  RCC    0  0  -0.3125        0  0  30.7925          1.309
c ---------- IRRADIAITON PORTS ---------
8  RCC  -30.5595    0  1.5875  28.8415 0  0   1.9           $ Port 1 - Steel
9  RCC  -30.5595    0  1.5875  28.8415 0  0   1.558         $ Port 1 - PMMA
10 RCC   1.718      0  1.5875  28.8415 0  0   1.9           $ Port 2 - Steel
11 RCC   1.718      0  1.5875  28.8415 0  0   1.558         $ Port 2 - PMMA
12 RCC   0  -30.5595  1.5875  0  28.8415 0   1.9           $ Port 3 - Steel
13 RCC   0  -30.5595  1.5875  0  28.8415 0   1.558         $ Port 3 - PMMA
14 RCC   0   1.718    1.5875  0  28.8415 0   1.9           $ Port 4 - Steel
15 RCC   0   1.718    1.5875  0  28.8415 0   1.558         $ Port 4 - PMMA
c ---------- PUBE SOURCE ---------------
16 RCC   0     0      0       0   0   3.30   1.308001  $ Source - Steel Encasing
18 RCC   0     0      0.5255  0   0  2.249   0.7824    $ Source - PuBe
c ---------- FOIL (In) -----------------
c        Foil x coordinate was changed to vary distance from the PuBe source.
17 RCC   3.308 0      1.5875  0.0127 0   0   1.27      $ In foil in Port 1
```

2

```
c --------------------------------------------------------------------------------
c ----------------------------- DATA CARDS ---------------------------------------
c --------------------------------------------------------------------------------
c
c   Data cards define the source, materials, and tallies. Tallies are the
c   desired outputs from the simulation.
c
c ------------------------- SOURCE DEFININION ---------------------------------
c
c  Particles are started within the rectangular sampling boundary - any particle
c  that is started within the boundary but not within the specified source cell
c  is terminated and not counted toward the tally.
c
c  In source definition, "d1" is described by "si1" and "sp1" cards
c                                          where "i" info, "p" probability
c
c  Energy spectra references:
c  Energy contributions pulled from SOURCES-4C model of PuBe source.
c
c
sdef cel=70          $ Define source cell as 70
     erg=d1          $ Define energy of source (neutron spectrum)
     x=d2 y=d3 z=d4  $ Sampling boundary
     par=n           $ Neutrons
     eff=0.01        $ Sampling efficiency (default)
c   Energy bins in MeV
si1 0 2.5E-8 5E-8 1E-7 5E-7 1E-6 1E-5 1E-4 1E-3 0.01 0.1 0.25 0.50 0.75 1.00
      1.25 1.50 1.75 2.00 2.25 2.50 2.75 3.00 3.25 3.50 3.75 4.00 4.25 4.50
      4.75 5.00 5.25 5.50 5.75 6.00 6.25 6.50 6.75 7.00 7.25 7.50 7.75 8.00
      8.25 8.50 8.75 9.00 9.25 9.50 9.75 10.00 10.25 10.50 10.75 11.00 11.25
      11.50 11.75 12.00
c   Fractional contributions to each energy bin
sp1 d 0 0 8.370E-32 0 4.932E-32 5.059E-32 0 8.901E-31 2.208E-10 5.159E-7
      4.586E-5 1.793E-4 5.008E-3 1.304E-2 1.703E-2 1.736E-2 1.544E-2 1.166E-2
      1.597E-2 1.938E-2 2.161E-2 2.654E-2 3.904E-2 5.015E-2 5.232E-2 5.013E-2
      4.722E-2 4.490E-2 4.311E-2 4.117E-2 3.878E-2 3.327E-2 2.723E-2 2.451E-2
      2.353E-2 2.039E-2 2.122E-2 2.400E-2 2.505E-2 2.503E-2 2.496E-2 2.440E-2
      2.302E-2 2.110E-2 1.932E-2 1.819E-2 1.741E-2 1.660E-2 1.464E-2 1.118E-2
      7.000E-3 3.951E-3 2.511E-3 1.264E-3 3.914E-4 6.322E-6 7.971E-29 6.330E-29
      5.014E-29
c   x_min   x_max
si2 -0.79   0.79    $ x-range limits for source volume
sp2  0      1       $ uniform probability over x-range
c   y_min   y_max
```

```
si3 -0.79   0.79
sp3  0      1
c    z_min  z_max
si4  0.52   2.78
sp4  0      1
c ---------------------------------------------------------------------------
c ----------------------------- TALLY -------------------------------------- 3
mode n                        $ Neutron mode
nps 1E+6                      $ Particle cutoff: 10^6
c
c  F4 tally for neutrons (n) in cell 80. F4 tally gives flux averaged over a
c  cell, normalized per source particle. Units of output are neutrons/cm^2 per
c  neutron. Output must be multiplied by PuBe yield (neutrons/s) to get units
c  of neutrons/cm^2 s.
c
F4:n 80
c
c  Tally output produced for the energy bins defined by E0. The neutron flux
c  below 5E-7 MeV will be printed along with the total neutron flux.
c
E0  5E-7  T                   $ Energy bins;
c
c  Tables 110, 10, and 50 are printed. Table 110 lists the starting histories
c  of the first 50 particles for verification. Table 10 lists the source
c  definitions. Table 50 lists the cell volumes, surface areas, and masses.
c
PRINT 110 10 50
c ---------------------------------------------------------------------------
c ---------------------------- MATERIALS ------------------------------------
c
c   Material information was gathered from Compendium of Material Composition
c   Data for Radiation Transport Modeling [46]. Materials follow the form:
c  mn   ZAID.id_i   fraction_i    $ Comments
c  where, n         = material #
c         ZAID      = nuclide identifier
c         .id_i     = neutron cross-section data table of nuclide i
c         fraction_i = fraction of nuclide i (negative = weight fraction,
c                     positive = atomic fraction)
c
c ---------------------------------------------------------------------------
c Paraffin Wax p = 0.930 g/cm^3  C25H52
m1      1001.70c  -0.148605    $ H
        6000.70c  -0.851395    $ C
c Polyvinyl Chloride (PVC) p = 1.406 g/cm^3  C2H3Cl
m2      1001.70c  -0.048382    $ H
        6000.70c  -0.384361    $ C
        17000.66c -0.567257    $ Cl
c Air p = 0.001205 g/cm^3
m3      6000.70c  -0.000124    $ C
        7014.70c  -0.755268    $ N
        8016.70c  -0.231781    $ O
        18000.59c -0.012827    $ Ar
c Stainless Steel 304 p = 8.00 g/cm^3
m4      6000.70c  -0.000400    $ C
        14000.60c -0.005000    $ Si
        15031.70c -0.000230    $ P
        16000.62c -0.000150    $ S
        24000.42c -0.190000    $ Cr
        25055.70c -0.010000    $ Mn
        26000.50c -0.701720    $ Fe
        28000.50c -0.092500    $ Ni
c Regular Concrete p = 2.30 g/cm^3
m5      1001.70c  -0.010000    $ H
        8016.70c  -0.532000    $ O
        11023.70c -0.029000    $ Na
        13027.70c -0.034000    $ Al
        14000.60c -0.337000    $ Si
```

```
        20000.62c -0.044000    $ Ca
        26000.50c -0.014000    $ Fe
c PMMA p = 1.18 g/cm^3  C5O2H8
m6      1001.70c  -0.080538    $ H
        6000.70c  -0.599848    $ C
        8016.70c  -0.319614    $ O
c Plutonium/Beryllium Source p = 2.918 g/cm^3  Fractions are not normalized
m7      94237.70c  1E-10       $ Pu-237
        94238.70c  5.451E-4    $ Pu-238
        94239.70c  5.486E-2    $ Pu-239
        94240.70c  1.013E-2    $ Pu-240
        94241.70c  4.946E-2    $ Pu-241
        94242.70c  8.787E-4    $ Pu-242
        04009.70c  9.288571E-1 $ Be
c Indium p = 7.31 g/cm^3
m8      49000.66c -1.00        $ In
```

# APPENDIX A.2 – MCNPX DOSE CODE

1

```
c ---------- IRRADIATION PORTS ---------
60   4  -8.00       -8   9   6 -2          imp:n=1 $ Port 1 - outer steel
61   3  -0.001205   -9   6  -2             imp:n=1 $ Port 1 - air
62   4  -8.00       -10  11  6 -2  12       imp:n=1 $ Port 2 - outer steel
63   3  -0.001205   -11  6  -2  17          imp:n=1 $ Port 2 - air
64   4  -8.00       -12  13  6 -2  8        imp:n=1 $ Port 3 - outer steel
65   3  -0.001205   -13  6  -2             imp:n=1 $ Port 3 - air
66   4  -8.00       -14  15  6 -2  8 10     imp:n=1 $ Port 4 - outer steel
67   3  -0.001205   -15  6  -2             imp:n=1 $ Port 4 - air
c ---------- PUBE SOURCE ---------------
70   7  -2.918      -18                    imp:n=1 $ PuBe Material
71   4  -8.00       -16  18                imp:n=1 $ Steel Encasing
c ---------- FOIL (In) -----------------
80   8  -7.31       -17                    imp:n=1 $ Indium
```

2

```
c ---------- IRRADIAITON PORTS ---------
8  RCC  -30.5595    0  1.5875  28.8415 0  0   1.9          $ Port 1 - Steel
9  RCC  -30.5595    0  1.5875  28.8415 0  0   1.558        $ Port 1 - Air
10 RCC   1.718      0  1.5875  28.8415 0  0   1.9          $ Port 2 - Steel
11 RCC   1.718      0  1.5875  28.8415 0  0   1.558        $ Port 2 - Air
12 RCC   0  -30.5595  1.5875  0  28.8415 0   1.9          $ Port 3 - Steel
13 RCC   0  -30.5595  1.5875  0  28.8415 0   1.558        $ Port 3 - Air
14 RCC   0   1.718    1.5875  0  28.8415 0   1.9          $ Port 4 - Steel
15 RCC   0   1.718    1.5875  0  28.8415 0   1.558        $ Port 4 - Air
c ---------- PUBE SOURCE ---------------
16 RCC   0     0      0       0   0   3.30   1.308001  $ Source - Steel Encasing
18 RCC   0     0      0.5255  0   0  2.249   0.7824    $ Source - PuBe
c ---------- FOIL (In) -----------------
c        Foil x coordinate was changed to vary distance from the PuBe source.
17 RCC   3.308 0      1.5875  0.0127 0   0   1.27       $ In foil in Port 1
```

3

```
c ------------------------------------------------------------------------------
c ------------------------------ TALLY -----------------------------------------
mode n                          $ Neutron mode
nps 1E+6                        $ Particle cutoff: 10^6
c
c  F4 tally for neutrons (n) in cell 80. F4 tally gives flux averaged over a
c  cell, normalized per source particle. Units of output are neutrons/cm^2 per
c  neutron. Output must be multiplied by PuBe yield (neutrons/s) to get units
c  of neutrons/cm^2 s.
c
F4:n 80
f5:n   -1.31   0 1.558 1.27
       -3.308  0 1.558 1.27
       -5.308  0 1.558 1.27
       -7.308  0 1.558 1.27
       -9.308  0 1.558 1.27
       -11.308 0 1.558 1.27
       -13.308 0 1.558 1.27
       -15.308 0 1.558 1.27
       -17.308 0 1.558 1.27
       -19.308 0 1.558 1.27
       -21.308 0 1.558 1.27
       -23.308 0 1.558 1.27
       -25.308 0 1.558 1.27
       -27.308 0 1.558 1.27
       -29.308 0 1.558 1.27
       -31.308 0 1.558 1.27
fc5     Ambient Dose Equivalent H*(10) in mrem/hr per n/s
```

```
e
e  Tally output produced for the energy bins defined by E0. The neutron flux
e  below 5E-7 MeV will be printed along with the total neutron flux.
e
E0  5E-7  T                    $ Energy bins;
c -------- ICRP-74 DCFs -----------------
c
c  Energy bins and corresponding H*(10), ambient dose equivalent conversion
c  factors from ICRP-74. DCFs are in units of mrem/hr per neutron/(cm^2 s).
c  Tally output will be in units of mrem/hr per n/s. These must be
c  multiplied by the PuBe yield to get the ambient dose equivalent in mrem/hr.
c
c -------- Energy Bins [MeV] -----------
de5  1.0E-9 1.0E-8 2.5E-8 1.0E-7 2.0E-7 5.0E-7 1.0E-6 2.0E-6 5.0E-6 1.0E-5
     2.0E-5 5.0E-5 1.0E-4 2.0E-4 5.0E-4 1.0E-3 2.0E-3 5.0E-3 1.0E-2 2.0E-2
     3.0E-2 5.0E-2 7.0E-2 1.0E-1 1.5E-1 2.0E-1 3.0E-1 5.0E-1 7.0E-1 9.0E-1
     1.0 1.2 2.0 3.0 4.0 5.0 6.0 7.0 8.0 9.0 10 12 14 15 16 18 20 30 50
     75 100 125 150 175 201
c -------- DCF [] ----------------------
df5  2.3760E-3 3.240E-3 3.8160E-3 4.6440E-3 4.860E-3 4.8960E-3 4.7880E-3
     4.6440E-3 4.320E-3 4.0680E-3 3.8160E-3 3.564E-3 3.3840E-3 3.2040E-3
     2.9880E-3 2.844E-3 2.7720E-3 2.8800E-3 3.780E-3 5.9760E-3 8.5320E-3
     1.4796E-2 2.160E-2 3.1680E-2 4.7520E-2 6.120E-2 8.3880E-2 1.1592E-1
     1.3500E-1 1.440E-1 1.4976E-1 1.5300E-1 1.512E-1 1.4832E-1 1.4688E-1
     1.4580E-1 1.440E-1 1.4580E-1 1.4724E-1 1.512E-1 1.5840E-1 1.7280E-1
     1.8720E-1 1.944E-1 1.9440E-1 2.0520E-1 2.160E-1 1.8540E-1 1.4400E-1
     1.1880E-1 1.026E-1 9.3600E-2 8.8200E-2 9.000E-2 9.3600E-2
```

# APPENDIX B

The results of the preliminary experiments are summarized in Appendix B. These experiments include the consistency check, with and without a motor (Appendix B.1), and the neutron activation analysis (Appendix B.2).

# APPENDIX B.1 – CONSISTENCY TEST

*Table B.1.1. Bare neutron flux of In foils in ports one through four.*

| **Bare Neutron Flux [neutrons cm$^{-2}$ s$^{-1}$] ($\varphi_{th}$)** | | | | | |
|---|---|---|---|---|---|
| **Distance [cm]** | **Port 1** | **Port 2** | **Port 3** | **Port 4** | ***P-Value*** |
| *Without Motor* | | | | | |
| 8.94 | 1901 ± 144 | 1909 ± 73.3 | 1921 ± 45.8 | 1879 ± 45.2 | *0.941* |
| 11.3 | 1272 ± 33.5 | 1092 ± 101 | 1067 ± 101 | 1139 ± 79.1 | *0.066* |
| 13.9 | 708.3 ± 36.6 | 775.8 ± 12.0 | 650.3 ± 21.4 | 665.9 ± 7.09 | *0.001* |
| 17.1 | 373.7 ± 2.75 | 347.4 ± 22.2 | 336.3 ± 35.6 | 335.7 ± 31.0 | *0.314* |
| *With Motor* | | | | | |
| 9.03 | 1912 ± 86.3 | 1973.2 ± 197 | 1991 ± 129 | 1742 ± 77.3 | *0.162* |
| 11.3 | 1247 ± 98.4 | 1249 ± 69.6 | 1324 ± 97.9 | 1293 ± 116.2 | *0.731* |
| 13.9 | 784.2 ± 38.2 | 730.7 ± 34.3 | 726.8 ± 23.5 | 747.1 ± 35.7 | *0.218* |
| 17.1 | 371.3 ± 32.9 | 357.1 ± 12.5 | 321.7 ± 12.6 | 335.7 ± 24.0 | *0.097* |

# APPENDIX B.2 – NEUTRON ACTIVATION ANALYSIS

*Table B.2.1. Bare, Cd, and thermal neutron flux for Dy foils in port 4, 11.3 cm from the PuBe source.*

| Foil | Neutron Flux [neutrons $cm^{-2}$ $s^{-1}$] | | |
|---|---|---|---|
| | Bare ( $\varphi_{bare}$ ) | Cd ( $\varphi_{Cd}$ ) | Thermal ( $\varphi_{th}$ ) |
| Dy-A | 1685 ± 220 | 6.994 ± 2.62 | 1605 ± 222 |
| Dy-B | 1685 ± 228 | 7.481 ± 3.45 | 1668 ± 232 |
| Dy-C | 1581 ± 214 | 6.342 ± 2.44 | 1566 ± 217 |
| Dy-D | 1551 ± 210 | 10.39 ± 3.63 | 1527 ± 214 |
| Average | 1610 ± 218 | 18.19 ± 3.04 | 1592 ± 221 |

*Table B.2.2. Net counts from bare, Cd, and thermal neutron flux used to determine foil mass through NAA.*

| Foil | Net Counts ($C$) | | | Mass (m) [mg][a] |
|---|---|---|---|---|
| | Bare | Cd | Thermal | |
| In-A | 34919 ± 1429 | 4275 ± 357 | 30644 ± 1787 | 199.8 ± 24.4 |
| In-B | 33174 ± 1062 | 4390 ± 127 | 28783 ± 1189 | 187.7 ± 21.5 |
| In-C | 36690 ± 459.3 | 4618 ± 436 | 32072 ± 895 | 209.1 ± 23.1 |
| In-D | 37758 ± 5460 | 4575 ± 358 | 33183 ± 358 | 216.3 ± 23.3 |

[a] *Mass determined through NAA*

*Table B.2.3. Mass of In determined from mass balance in Eqn. 2.3.*

| Foil | Total Mass [mg] | Thickness [cm] | Mass of Indium [mg] |
|---|---|---|---|
| In-A | 642.2 ± 0.10 | 0.029 ± 0.001 | 389 ± 21.7 |
| In-B | 641.7 ± 0.10 | 0.030 ± 0.001 | 367 ± 21.7 |
| In-C | 634.9 ± 0.10 | 0.028 ± 0.001 | 399 ± 21.7 |
| In-D | 630.0 ± 0.10 | 0.032 ± 0.001 | 305 ± 21.7 |

# APPENDIX C

# THERMAL NEUTRON CHARACTERIZATION TABLES FOR INDIUM

*Table C.1. Thermal neutron flux characterization for port one.*

| Port 1 | | | |
|---|---|---|---|
| Distance [cm] | Neutron Flux [neutrons $cm^{-2}$ $s^{-1}$] | | |
| | Bare ( $\varphi_{bare}$ ) | Cd ( $\varphi_{Cd}$ ) | Thermal ( $\varphi_{th}$ ) |
| 3.99 | 5506 ± 552 | 1108 ± 111 | 4398 ± 663 |
| 16.7 | 656.4 ± 66.0 | 78.56 ± 8.15 | 577.8 ± 74.1 |

*Table C.2. Thermal neutron flux characterization for port two.*

| Port 2 | | | |
|---|---|---|---|
| Distance [cm] | Neutron Flux [neutrons $cm^{-2}$ $s^{-1}$] | | |
| | Bare ( $\varphi_{bare}$ ) | Cd ( $\varphi_{Cd}$ ) | Thermal ( $\varphi_{th}$ ) |
| 8.69 | 3195 ± 320 | 482.1 ± 49.6 | 2713 ± 369 |
| 13.7 | 1140 ± 114 | 148.8 ± 15.2 | 991.0 ± 130 |

*Table C.3. Thermal neutron flux characterization for port three.*

| Port 3 | | | |
|---|---|---|---|
| Distance [cm] | Neutron Flux [neutrons $cm^{-2}$ $s^{-1}$] | | |
| | Bare ( $\varphi_{bare}$ ) | Cd ( $\varphi_{Cd}$ ) | Thermal ( $\varphi_{th}$ ) |
| 3.58 | 5988 ± 600 | 1055 ± 106 | 4933 ± 706 |
| 9.04 | 2706 ± 271 | 397 ± 40.0 | 2309 ± 311 |

*Table C.4. Thermal neutron flux characterization for port four.*

| Port 4 | | | |
|---|---|---|---|
| Distance [cm] | Neutron Flux [neutrons $cm^{-2}$ $s^{-1}$] | | |
| | Bare ( $\varphi_{bare}$ ) | Cd ( $\varphi_{Cd}$ ) | Thermal ( $\varphi_{th}$ ) |
| 3.58 | 5895 ± 591 | 1077 ± 108 | 4819 ± 699 |
| 8.69 | 3355 ± 336 | 509.2 ± 51.5 | 2846 ± 388 |
| 13.7 | 1203 ± 121 | 150.3 ± 15.3 | 1052 ± 136 |

# REFERENCES


1. Bechtel, R. D. (2007). Uranium-232 beryllide neutron source. Master of Science in Nuclear and Radiological Engineering Thesis, Georgia Institute of Technology.

2. Oudah, O. N. (2015). Determine neutron yield from beryllium compounds bombarding with alpha particles. International Journal of Scientific & Technology Research, 4(4), 82-84.

3. Lorch, E. A. (1973). Neutron spectra of 214Am/B, 241Am/Be, 241Am/F, 242Cm/Be, 238Pu/13C and 252Cf isotopic neutron sources. The International Journal of Applied Radiation and Isotopes, 24(10), 585-591. doi:10.1016/0020-708X(73)90127-0.

4. Anderson, M. E., & Neff, R. A. (1972). Neutron energy spectra of different size 239Pu-be(α,n) sources. Nuclear Instruments and Methods, 99(2), 231-235. doi:10.1016/0029-554X(72)90781-1.

5. Bair, J. K., & Campo, J. G. (1979). Neutron yields from alpha-particle bombardment. Nuclear Science and Engineering, 71(1), 18-28. doi:10.13182/NSE71-18.

6. Molina, F., Aguilera, P., Romero-Barrientos, J., Arellano, H. F., Agramunt, J., Medel, J., et al. (2017). Energy distribution of the neutron flux measurements at the chilean reactor RECH-1 using multi-foil neutron activation and the expectation maximization unfolding algorithm. Applied Radiation and Isotopes, 129, 28-34. doi:10.1016/j.apradiso.2017.08.001.

7. Knoll, G. F. (2000). Radiation detection and measurement (Third ed.). US: John Wiley & Sons, Inc.

8. Chadwick, M. B., Herman, M., Obložinský, P., Dunn, M. E., Danon, Y., Kahler, A. C., et al. (2011). ENDF/B-VII.1 nuclear data for science and technology: Cross sections, covariances, fission product yields and decay data. Nuclear Data Sheets, 112(12), 2887-2996. doi:10.1016/j.nds.2011.11.002.

9. Reactor Experiments Inc. (1965). Activation foil manual: Neutron activation foils (Instruction Manual). Sunnyvale, CA: Reactor Experiments, Inc. (Activation Foil Manual).

10. Rosman, K. J. R., & Taylor, P. D. P. (1998). Isotopic compositions of the elements 1997 (technical report). Pure and Applied Chemistry, 70(1), 217-235. doi:10.1351/pac199870010217.

11. Bruin, M. (1983). Instrumental neutron activation analysis - a routine method. (Thesis, Delft University of Technology). 15 (11) Retrieved from http://inis.iaea.org/search/search.aspx?orig_q=RN:15035293.

12. Powell, J. E., & Walker, J. V. (1964). A determination of the cadmium absorption of resonance neutrons in cadmium-covered indium foils. Nuclear Science and Engineering, 20(4), 476-480. doi:10.13182/NSE64-A20990.

13. Pierce, C. R., & Shook, D. F. (1967). Determination of tungsten resonance absorption integrals by activation (Technical Report No. NASA-TN-D-4137). Cleveland, OH: United States. (Cadmium cut-off in tungsten).

14. Osae, E. K., Nyarko, B. J. B., Serfor-Armah, Y., & Akaho, E. H. K. (1998). An alternative method for the measurement of thermal neutron flux (modified cadmium ratio method). Journal of Radioanalytical and Nuclear Chemistry, 238(1-2), 105-110. doi:10.1007/BF02385363.

15. Mueck, K., & Bensch, F. (1973). Cadmium correction factors of several thermal neutron foil detectors. Journal of Nuclear Energy, 27(9), 677-688. doi:10.1016/0022-3107(73)90025-7.

16. Oak Ridge Associated Universities. (2007). Proportional counters. Retrieved from https://www.orau.org/ptp/collection/proportional%20counters /introprops.htm.

17. Steinmeyer, P. R. (2005). G-M pancake detectors: Everything you've wanted to know (but were afraid to ask). RSO Magazine, 10(5), 7-17.

18. Pelowitz, D. B. (2011). MCNPX user's manual (User Manual No. LA-CP-11-00438). Oak Ridge, TN: U.S. Department of Energy.

19. Oak Ridge National Laboratory. (2013). RSICC computer code collection: MCNP6.1/MCNP5/MCNPX (Technical Report No. CCC-810). Oak Ridge, TN: U.S. Department of Energy.

20. Shultis, J. K., & Faw, R. E. (2011). An MCNP primer: An introduction to the MCNP code. Manhattan, KS: Kansas State University.

21. Hall, E. J., & Giaccia, A. J. (2012). Radiobiology for the radiologist (Seventh ed.). Philadelphia, PA: Lippincott Williams & Wilkins.

22. Choppin, G., Liljenzin, J., Rydberg, J., & Ekberg, C. (2013). Chapter 8 - radiation effects on matter. In G. Choppin, J. Liljenzin, J. Rydberg & C. Ekberg (Eds.), Radiochemistry and nuclear chemistry (Fourth ed., pp. 209-237). Oxford: Academic Press. doi:10.1016/B978-0-12-405897-2.00008-2.

23. International Commission on Radiological Protection. (2003). Relative biological effectiveness (RBE), quality factor (Q), and radiation weighting factor ($w_R$). ICRP Publication 92. Annals of the ICRP, 33(4).

24. Vana, N., Hajek, M., & Berger, T. (2003). Ambient dose equivalent H*(d) - an appropriate philosophy for radiation monitoring onboard aircraft and in space? Paper presented at the Bratislava, Slovakia. 6(42), 1-4.

25. International Commission on Radiological Protection. (2007). The 2007 recommendations of the international commission on radiological protection. ICRP Publication 103. Annals of the ICRP, 37(2-4).

26. International Commission on Radiological Protection. (1996). Conversion coefficients for use in radiological protection against external radiation. Annals of the ICRP, 26(3), 1-205.

27. Papastefanou, C. (2004). Measurement of neutron flux and albedo of water for thermal neutrons with foils of indium in a subcritical nuclear reactor. Journal of Radioanalytical and Nuclear Chemistry, 261(3), 671-678. doi:10.1023/B:JRNC.0000037112.08894.21.

28. Freeman, K. R. (2010). Flux mapping of a 239Pu/Be source by neutron activation analysis. Unpublished manuscript.

29. Harvey, Z.R. (2010). Neutron flux and energy characterization of a plutonium-beryllium isotopic neutron source by Monte Carlo simulation with verification by neutron activation analysis. UNLV Theses, Dissertations, Professional Papers, and Capstones. 900.

30. Shores, E. F. (1999). Calculated dose equivalent rates from PuBe source neutrons. Transactions of the American Nuclear Society, 31(12), 243-245.

31. Tate, R. E., & Coffinberry, A. S. (1958). Plutonium-beryllium neutron sources their fabrication and their yield (Technical Report No. A/CONF.15/P/700). United States: USDOE.

32. Rawls, W. S., & Voss, H. G. (1966). A versatile, inexpensive neutron howitzer. American Journal of Physics, 34(12), 1182-1184. doi:10.1119/1.1972574.

33. Anderson, M. E. (1968). Increases in neutron yields of plutonium-beryllium (α,n) sources. Nuclear Applications, 4(3), 142-147. doi:10.13182/NT68-A26377.

34. Perry, R. T., & Pearson, M. (2000). Encapsulation and source activities of alpha-N neutron sources. Paper presented at the Topical Meeting on Radiation Protection for our National Priorities: Medicine, the Environment, and the Legacy, American Nuclear Society, Radiation Protection and Shielding Division, Spokane, WA. pp. 743-749. Retrieved from /z-wcorg/ database.

35. Nguyen, C. T. (2006). Verification of the content, isotopic composition and age of plutonium in pu-be neutron sources by gamma-spectrometry. Nuclear Instruments and Methods B, 251(1), 227-236.

36. Mughabghab, S. F. (2018). Recommended thermal cross sections, resonance properties, and resonance parameters for Z = 61–102. In S. F. Mughabghab (Ed.), Atlas of neutron resonances (Sixth ed., pp. 111-679). Amsterdam: Elsevier. doi:10.1016/B978-0-44-463780-2.00015-3.

37. Geiger, K. W., & Van Der Zwan, L. (1975). Radioactive neutron source spectra from 9Be(α, n) cross section data. Nuclear Instruments and Methods, 131(2), 315-321. doi:10.1016/0029-554X(75)90336-5.

38. Ali, S., Laherty, M., Laprade, J. W., Cala, P. M., Lipschultz, F. P., & Neuhauser, B. (2015). A portable shield for a neutron howitzer used for instructional and research purposes. Applied Radiation and Isotopes, 103, 37-42. doi:10.1016/j.apradiso.2015.05.011.

39. De Laeter, J. R., Bohlke, J. K., De Bievre, P., Hidaka, H., Peiser, H. S., Rosman, K. J. R., et al. (2003). Atomic weights of the elements: Review 2000. International Union of Pure and Applied Chemistry, 75(6), 683-800.

40. P.J. Linstrom and W.G. Mallard, Eds. NIST Chemistry WebBook, NIST Standard Reference Database Number 69. National Institute of Standards and Technology. Gaithersburg MD, 20899. https://doi.org/10.18434/T4D303.

41. Mughabghab, S. F. (2018). Recommended thermal cross sections, resonance properties, and resonance parameters for Z = 1–60. In S. F. Mughabghab (Ed.), Atlas of neutron resonances (Sixth ed., pp. 89-822). Amsterdam: Elsevier. doi:10.1016/B978-0-44-463769-7.00015-4.

42. Blachot, J. (2010). Interactive Chart of Nuclides. NNDC Brookhaven National Laboratory. https://www.nndc.bnl.gov/chart/.

43. Gamma Products, Inc. (2017). G5020 Traveler User's Manual.

44. Cooper, P. N., & Kabir, S. M. (1972). Calibration of threshold activation detectors with 14 MeV neutrons. Nuclear Instruments and Methods, 104(1), 227-229. doi:10.1016/0029-554X(72)90325-4.

45. Stuart, D. C., Ryan, D. E. (1981). Epithermal neutron activation analysis with a SLOWPOKE nuclear reactor. Canadian Journal of Chemistry, 59(10), 1470-1475. doi: 10.1139/v81-215.

46. McConn Jr., R. J., Gesh, C. J., Pagh, R. T., Rucker, R. A., Williams III, R. G. (2011). Compendium of Material Composition Data for Radiation Transport Modeling. Pacific Northwest National Laboratory. PNNL-15870, Rev. 1.

47. Anyenda, O.E. (2009). Characterization and application of neutron flux of a 370 GBq $^{241}$Am-Be irradiating system. Masters of Science Thesis, University of Nairobi.

48. Graham, J., Landsberger, S., Ferreira, P.J., Ihlefeld, J., Brennecka, G. (2012). Characterization of Neutron Flux Spectra for Radiation Effects Studies. Journal of Radioanalytical and Nuclear Chemistry, 291(2), 503-507. doi:10.1007/s10967-011-1270-0.

49. Suman, V., Tripathy, S.P., Sunil, C., Shanbhag, A.A., Paul, S., Sahoo, G.S., Bandyopadhyay, T., Sarkar, P.K. (2016). Measurement of Neutron Energy Distributions From p+Be Reaction at 20 MeV Using Threshold Activation Foils. IEEE Transactions on Nuclear Science, 63(4), 2283-2292. doi:10.1109/TNS.2016.257 2728.

50. Zsolnay, E.M., Szondi, E.J. (1982). Neutron Spectrum Determination by Multiple Foil Activation Method. Periodica Polytechnica Electrical Engineering (Archives), 26(1-2), 31-46. https://pp.bme.hu/ee/article/view/4744.

51. Halstead, M.R., Lee, S., Petrosky, J., Bickley, A., Sokol, P. (2012). Neutron energy spectrum characterization on TMR-1 at the Indiana University neutron source. Physics Procedia, 26(2012), 188-195.

52. Stefanik, M., Bem, P., Majerle, M., Novak, J., Simeckova, E. (2017). Neutron spectrum determination of d(20)+Be source reaction by the dosimetry foils method. Radiation Physics and Chemistry, 140(2017), 466-470. doi:10.1016/j.radphyschem.2017.03.029.

53. Kulage, Z.A. (2010). Characterization of the neutron flux spectrum at the Missouri University of Science Technology Research Reactor. Masters Thesis (4753).